Influence of High Cycle Thermal Loads on Thermal Fatigue Behavior of Thick Thermal Barrier Coatings

Dongming Zhu and Robert A. Miller

19970616 064

U.S. ARMY

RESEARCH LABORATORY

Influence of High Cycle Thermal Loads on Thermal Fatigue Behavior of Thick Thermal Barrier Coatings

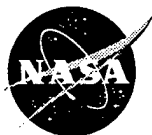Dongming Zhu and Robert A. Miller
Lewis Research Center
Cleveland, Ohio

INFLUENCE OF HIGH CYCLE THERMAL LOADS ON THERMAL FATIGUE BEHAVIOR OF THICK THERMAL BARRIER COATINGS

Dongming Zhu [†] and Robert A. Miller
National Aeronautics and Space Administration
Lewis Research Center, Cleveland, OH 44135

ABSTRACT

Thick thermal barrier coating systems in a diesel engine experience severe thermal low cycle fatigue (LCF) and high cycle fatigue (HCF) during engine operation. In the present study, the mechanisms of fatigue crack initiation and propagation, as well as of coating failure, under thermal loads which simulate engine conditions, are investigated using a high power CO_2 laser. In general, surface vertical cracks initiate early and grow continuously under LCF and HCF cyclic stresses. It is found that in the absence of interfacial oxidation, the failure associated with LCF is closely related to coating sintering and creep at high temperatures, which induce tensile stresses in the coating after cooling. Experiments show that the HCF cycles are very damaging to the coating systems. The combined LCF and HCF tests produced more severe coating surface cracking, microspallation and accelerated crack growth, as compared to the pure LCF test. It is suggested that the HCF component cannot only accelerate the surface crack initiation, but also interact with the LCF by contributing to the crack growth at high temperatures. The increased LCF stress intensity at the crack tip due to the HCF component enhances the subsequent LCF crack growth. Conversely, since a faster HCF crack growth rate will be expected with lower effective compressive stresses in the coating, the LCF cycles also facilitate the HCF crack growth at high temperatures by stress relaxation process. A surface *wedging* model has been proposed to account for the HCF crack growth in the coating system. This mechanism predicts that HCF damage effect increases with increasing temperature swing, the thermal expansion coefficient and the elastic modulus of the ceramic coating, as well as the HCF interacting depth. A good agreement has been found between the analysis and experimental evidence.

[†] National Research Council — NASA Research Associate at Lewis Research Center.

INTRODUCTION

Ceramic thermal barrier coatings have attracted increasing attention in heat engines because of their ability to provide thermal insulation to engine components. The advantages of using the ceramic coatings include a potential increase in engine operating temperature with elimination of the water cooling system and a longer service life in the harsh in-cylinder environment. ZrO_2-based ceramics are the most important coating materials for such applications because of their low thermal conductivity, relatively high thermal expansivity and excellent mechanical properties. A typical thermal barrier coating system consists of a top layer ZrO_2-8%Y_2O_3 coating and an intermediate superalloy-type bond coat and the alloy substrate. The application of advanced thick thermal barrier coatings (TTBCs) for diesel engine components such as piston crowns and cylinder heads is promising for increasing engine fuel efficiency, performance and reliability [1, 2].

However, durability of thick thermal barrier coatings under severe temperature cycling conditions encountered in a diesel engine remains a major problem. In a diesel engine, two types of thermal fatigue transients exist [1, 3, 4]. The first transient type, which is associated with the start/stop and no-load/full-load engine cycle, generates thermal low cycle fatigue (LCF) in the coating system. The second transient type, which is associated with the in-cylinder combustion process, generates a thermal high cycle fatigue (HCF). It occurs at a frequency on the order of 10 Hz (i.e., 1000-2600 RPM). The HCF transient can generate a temperature fluctuation of more than 200°C that will superimpose onto the steady-state engine temperature at the coating surface [1, 3, 5]. Therefore, the failure mechanisms of thick thermal barrier coatings are expected to be quite different from those of thin TBCs under these temperature transients. The coating failure is related not only to thermal expansion mismatch and oxidation of the bond coats and substrates [2, 6, 7], but also to the steep thermal stress gradients induced from the temperature distributions during the thermal transients in the coating systems [1, 2, 7-10].

The development of advanced thick thermal barrier coatings requires a thorough understanding of thermal fatigue behavior. Although it has been reported [8, 11] that stresses generated by a thermal transient can initiate surface and interface cracks in a coating system, the mechanisms of the crack propagation and of coating failure under the complex LCF and HCF conditions are still not understood. Particularly, the understanding of surface vertical crack propagation in thick thermal barrier coatings under thermal cyclic loading is of great importance. Experimental evidence has shown all coating failure under severe

thermal cycling conditions, produced either by a high heat flux burner rig or a high power laser, is more or less associated with surface vertical cracks [7, 12]. These vertical surface cracks and sometimes through-thickness-cracks can facilitate the interfacial crack formation, eventually resulting in the coating delamination and spallation. In addition, the interaction between LCF and HCF cycles, and the impact of relative amplitude of the LCF and HCF transients on coating fatigue life are among the most important aspects in understanding the thermal fatigue behavior of the coating systems. In this paper, thermal fatigue behavior of an yttria partially stabilized zirconia coating system under simulated LCF and HCF engine conditions is investigated. The effects of LCF and HCF parameters on surface fatigue crack initiation and propagation in the coating are also discussed.

EXPERIMENTAL MATERIALS AND METHODS

Materials and Specimen Preparation

ZrO_2-8 wt % Y_2O_3 ceramic coating and Fe-25Cr-5Al-0.5Y bond coat were plasma-sprayed onto 4140 and 1020 steel substrates using an ABB ASEA IFB2000 6-axis industrial robot. The plasma spray conditions used for both the ceramic coating and bond coat are listed in Table 1. The sample substrate configurations were rectangular bar, as well as angle iron which provided a corner shape for the coating. The specimen dimensions are illustrated in Figure 1. The thickness of the ceramic coating was about 1.5-1.6 mm. The bond coat thicknesses were 0.28 mm and 0.5 mm for the angle iron specimens and the rectangular flat specimens, respectively.

Table 1 Plasma spray parameters for ZrO_2-8wt%Y_2O_3 top coat and FeCrAlY bond coat

Coatings materials	Torch power KW	Plasma gas flow rate Standard liter/min.	Carrier gas flow Standard liter/min.	Spray distance mm	Feed rate g/min.	Torch translation rate mm/s	Air cooling condition Psi	Substrate temperature °C
FeCrAlY PRAX-AIR FE213 44-74 μm	35 (9mB plasma torch, GH nozzle)	Ar: 56.6 N$_2$: 9.4	Ar: 8.3	127	68	1300	50	250
ZrO_2-8%Y_2O_3 ZIRCOA 9507/46 44-74 μm	40 (9mB plasma torch, GH nozzle)	Ar: 14.2 N$_2$: 7.1	Ar: 3.2	101.6	20	1000	50	250

ceramic

bond coat

substrate

unit: mm

1.5 KW CO_2 cw Industrial Laser

8 micron pyrometers

203

t_c

t_b=0.285

(a) Angle iron specimen

25

t_s=5.66

4.0

90°

Thermocouple

Air

t_c

t_s=12.7

t_b=0.5

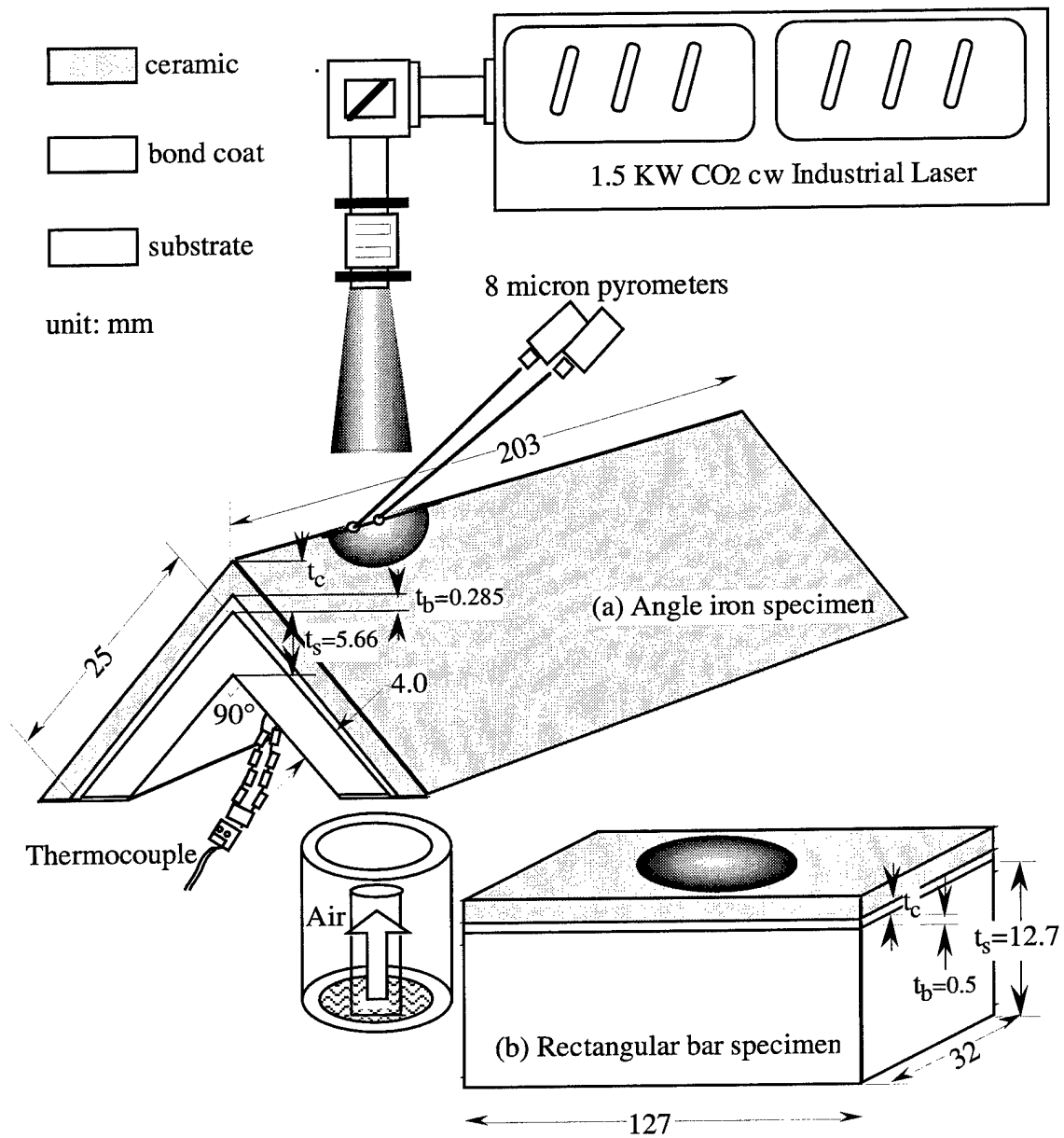(b) Rectangular bar specimen

32

127

Fig. 1   Schematic diagram showing two specimen geometries.

Low Cycle and High Cycle Fatigue Tests

Low cycle and high cycle fatigue tests under simulated engine temperature and stress conditions were conducted using a high power 1.5 KW CO_2 laser (EVERLASE, Coherent General Inc., Massachusetts). This test rig was controlled by a PC programmed to simulate different LCF and HCF temperature cycles. In this study, the HCF combustion cycles were simulated using the pulsed laser mode. The laser pulse period and pulse width were set at 92 and 9 milliseconds (ms) respectively, with effective square wave equivalent pulse heating time about 6 ms. The total beam power in the pulsed mode was set to approximately 180W. The laser pulse input waveform, measured by an oscilloscope (THS 720 Tekscope with frequency 100 MHz and data acquisition rate 500 Meg samples/sec., Tektronix, Oregon), is shown in Figure 2.
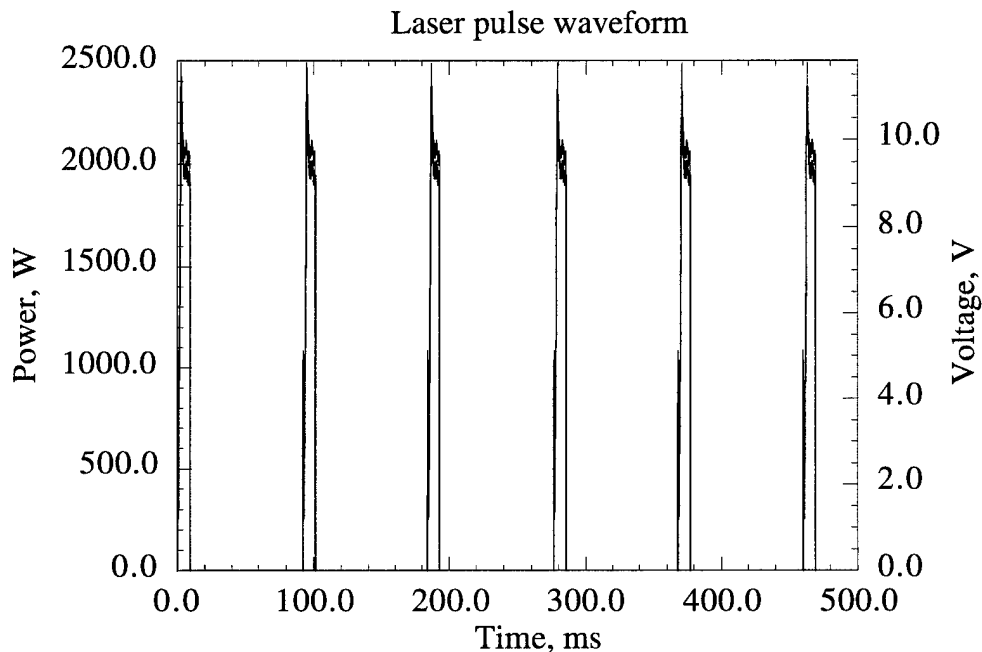

Fig. 2 Laser pulse waveform recorded from the laser pulse signal by THS 720 Tekscope.

The laser power density for an idealized spherical Gaussian beam is related to laser total power P and beam radius w by the following relation [13, 14]

$$I(r) = I_0 \exp\left(\frac{-2r^2}{w}\right) = \frac{2P}{\pi w^2} \exp\left(\frac{-2r^2}{w}\right) \qquad (1)$$

where I_0 is laser power density at the center, r is the distance from the center. The beam radius w has been defined as the distance at which the laser power density has dropped to $1/e^2$ of its value at the center. In this study, in order to produce a lower power density suitable for simulating diesel engine conditions, and also to cover a larger test specimen area, a Plano Concave ZeSe lens with focal length -330 mm was used to expand the laser beam. With the specimen being placed at a distance 460 mm from the magnifying lens, the beam radius w was increased from 7 mm to about 16 mm, as determined from laser burn patterns. Laser power density distributions under the test conditions are shown in Figure 3.

———— Expanded beam, pulse mode   -------- Raw beam, pulse mode
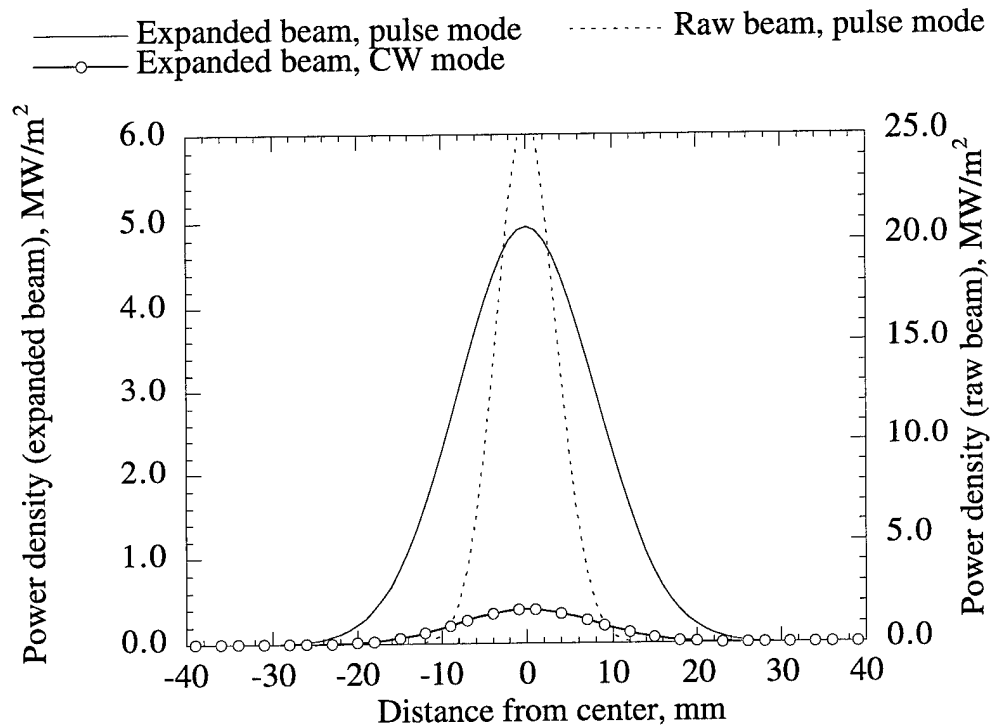—o— Expanded beam, CW mode

Fig. 3   Laser power density distributions estimated from the measured laser waveform and total power output. Minor beam non-uniformity observed is neglected.

During the thermal fatigue testing, specimen surface temperatures were measured by two 8 micron infrared Pyrometers (Model MX-M803 Maxline Infrared Thermometer Measurement and Control System, Ircon, Inc., Illinois), aimed at the beam center (giving the peak temperature) and 7 mm away from the center, as shown in Figure 1. The backside metal temperature was determined by an R-type thermocouple. For the combined LCF and HCF tests, the pulsed laser mode was used to generate the heating and cooling cycles, and the total power output was 180W. Two sets of experiments were conducted for angle iron specimens, with heating/cooling cycle times set at 30/5 and 5/3 minutes respectively. Because the high energy laser pulse was used, an HCF component was inherently

superimposed on the LCF cycles. These experiments were designed to provide information on LCF and HCF interactions, and the effect of relative LCF and HCF cycle numbers on ceramic coating failure mechanisms. Backside air cooling was used to maintain the desired temperature gradient. The backside metal temperature was fixed at about 250°C, by simply adjusting the cooling air flow. Steady state heating was usually reached in two to three minutes. The peak specimen surface temperature (steady-state average temperature at the beam center location) thus measured was about 850°C. The total HCF cycle numbers were fixed at 10×10^6 cycles for the angle iron specimens, corresponding to a total heating time of about 256 hours. In order to study the effect of surface temperature on fatigue behavior, another angle iron test was conducted of using a backside temperature fixed at 350°C, with a corresponding surface center temperature about 950°C. A pure LCF test was also conducted using the continuous wave (CW) laser, with a same total power 180W and a 5 minute heating and 3 minute cooling cycle, to study coating fatigue behavior in the absence of an HCF component. A similar set of pure LCF and combined LCF and HCF tests were also carried out for the rectangular flat specimens. With a fixed back temperature of 250°C, the 180W pulsed laser beam generated a surface center temperature of approximately 920°C. The tests were used to provide information on crack distributions and coating fatigue behavior of flat specimens. The specimen and experimental conditions for LCF and HCF tests are summarized in Table 2.

Table 2. Summary of specimen and experimental conditions

No	Material	Test type	Surface tempera- ture °C	Backside metal tempera- ture °C	Heating/ cooling time, min.	Total heating time hrs.	Total HCF cycles $\times 10^6$	Total LCF cycles
1	Angle iron TBC tc=1.6mm tb=0.28mm	LCF CW 180W	850	250	5/3	256	–	3067
2	Angle iron TBC tc=1.6mm tb=0.28mm	LCF& HCF Pulse 180W	850	250	30/5	256	10	510
3	Angle iron TBC tc=1.6mm tb=0.28mm	LCF& HCF Pulse 180W	850	250	5/3	256	10	3067
4	Angle iron TBC tc=1.6mm tb=0.28mm	LCF& HCF Pulse 180W	950	350	30/6	256	10	510
5	Flat TBC tc=1.5mm tb=0.5mm	LCF& HCF Pulse 180W	920	250	30/5	153	6	307
6	Flat TBC tc=1.5mm tb=0.5mm	LCF CW 180W	920	250	30/5	153	–	307

Since the pyrometer has a slower response time (> 25 ms) compared to the actual laser pulse width (6 ms), the temperature swing generated by the pulsed laser on the ceramic surface could not be recorded. Therefore, one dimensional finite difference analysis has been used to model the thermal HCF temperature profile, providing the important thermal parameters such as the temperature fluctuation ΔT and interaction depth on the ceramic surface under the given test conditions.

Microscopic Examinations

The tested coating surfaces and cross-sections were examined under both optical and electron scanning microscopes to obtain information on crack density and distribution, as well as crack surface morphology. To prevent damage by specimen cross-section preparation, a pressurized epoxy infiltration method for specimen mounting was used. By this technique, epoxy was first poured over the specimens and their holding cups in a vacuum chamber. After the epoxy degassing in vacuum, the specimens were moved into a pressurized chamber (up to 1200 Psi) for 24 hours, as the epoxy cured. Therefore, the epoxy filled the cracks in the specimen, and the original crack characteristics generated in thermal fatigue tests were preserved.

EXPERIMENTAL RESULTS

Temperature Cycles Induced by Laser Beam Heating

Figure 4 shows typical temperature cycles of laser thermal fatigue tests. The steady states were reached during the first few minutes of the cycling. It may be noticed that under the combined LCF and HCF conditions, even though the pyrometer could not accurately read the temperature fluctuations of the HCF component because of its slow response time, large variations in recorded temperatures were still observed during laser heating. In contrast, the continuous wave laser test simulating the pure LCF condition showed very little temperature fluctuation. This suggests that regardless of the similar steady state average temperature profiles produced by the pulsed laser beam and the CW laser beam, the pulsed laser beam heating induced a severe surface temperature swing which was superimposed onto the steady state temperature.

Because of an expanded near-Gaussian laser beam used, temperature distributions are expected to vary across the beam diameter. This was confirmed by experiments, as shown in Figure 4. The average temperature reading from the pyrometer aimed at a point

7 mm away from the center is 250°C lower than that from the pyrometer aimed at the center for the angle iron specimens. Even higher temperature differences were observed for the flat specimens. This Gaussian beam profile, in principle, can provide additional information on coating failure mechanisms with heat flux distributions, establishing a relationship between the coating damage and the test parameters, such as the average surface temperature and temperature swing from a set of experiments.

Temperature and Thermal Stress Distributions

Figure 5 shows the calculated temperature distributions (with a simplified one-dimensional configuration) across the thermal barrier coating system on an angle iron during the steady state heating under various heat fluxes. Because of the constraints imposed by the angle iron structure, specimen bending was not likely to occur. Therefore, the in-plane stress distributions in the system at the steady state during the first heat up could be calculated from the mechanical equilibrium and strain compatibility conditions. The results are shown in Figure 6. The material properties used in the calculations are listed in Table 3. It should be noted that the overall stress is the summation of the thermal stress and residual stress in the system. As will be discussed later, for longer heating times, ceramic sintering and creep will become significant, thus modifying the stress states in the coating system.

When pulsed laser heating is used, a severe thermal transient will be induced even in the absence of LCF cycling. This temperature fluctuation and history under the HCF conditions were modeled by the one dimensional finite difference approach. In order to verify the validity of this model under the present laser beam conditions, the one dimensional finite difference analysis method was compared with analytical solutions for both a uniform, constant irradiance model and a Gaussian beam model in calculating the surface temperature swing [12]. The temperature swing predicted by all three approaches was essentially the same, implying that the Gaussian beam is sufficiently widespread to allow the use of the one-dimensional assumption. The modeled results indicate that the HCF transient occurs only at the surface layer of the ceramic coating. This layer may be defined as the HCF interaction depth at which appreciable temperature fluctuation (20°C or above) will occur. This temperature swing generated by the pulsed laser increases with increasing the laser peak power density and the laser pulse width (laser pulse heating time), as shown in Figure 7. However, the HCF interaction layer depth, which is independent of laser power density, increases with increasing laser pulse width, as illustrated in Figure 8. Under the HCF condition of 6 ms heating, the interaction depth is about 0.15 mm, as

calculated by the finite difference method. The HCF component, therefore, is generated only on the very surface of the ceramic coating. However, the effect of HCF on thermal fatigue is more complex and will extend far beyond this characteristic depth, as will be discussed later.

The temperature profiles generated by the pulsed laser under peak heat fluxes 3.38 and 4.95 MW/m^2 are illustrated in Figure 9. The HCF stress distributions with coating depth and variations with time are shown in Figure 10. It can be seen that this temperature fluctuation induces high-frequency cyclic stresses on the coating surface, with the predicted HCF stress ranging from around 60 MPa at 3.38 MW/m^2 to 100 MPa at 4.95 MW/m^2. The dashed lines in Figure 10 represent the ceramic surface stress values at the average steady state surface temperatures under the corresponding average heat fluxes 0.220 and 0.323 MW/m^2, respectively.

Table 3 Physical and mechanical properties of the thermal barrier coating system used in calculations

Material Properties	Plasma sprayed ZrO$_2$-8%Y$_2$O$_3$	Plasma sprayed FeCrAlY	Steel substrate
Thermal conductivity k, W/m·K	0.9	11.0	46.7
Thermal expansion coefficient α, m/m·°K	10.8×10^{-6}	12.4×10^{-6} m/m°C	14.2×10^{-6} m/m°C
Density ρ, kg/m^3	5236	–	7850
Heat capacity c, J/kg·K	582	–	456.4
Young's modulus E, GPa	27.6	137.9	207.0
Poisson's ratio, V	0.25	0.27	0.25
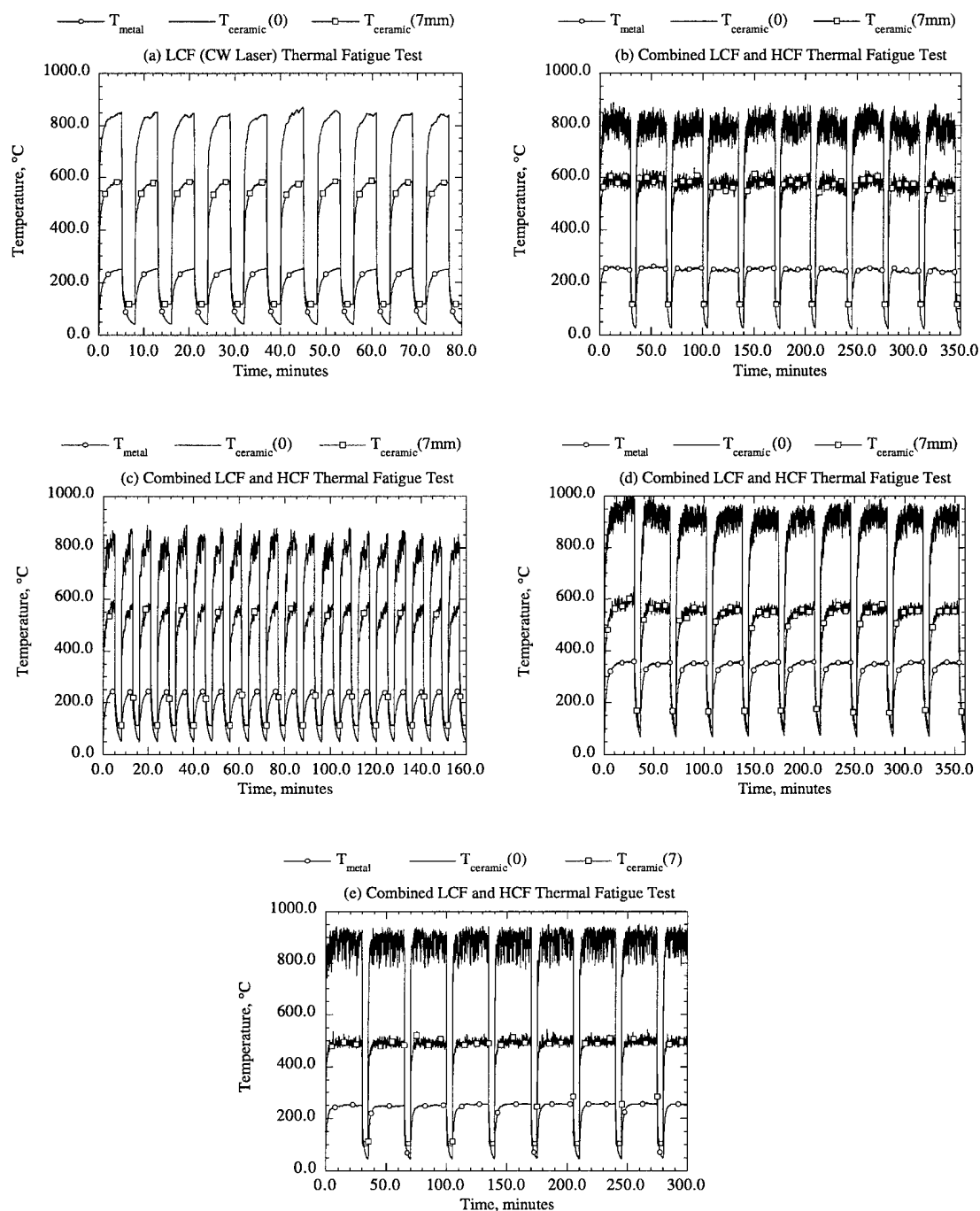
Fig. 4   Laser heating and cooling profiles simulating the engine operating conditions (temperature has been corrected with angle iron configurations). (a) Angle iron with LCF only; (b), (c) and (d) Angle iron with combined LCF and HCF; (e) Flat specimen with combined LCF and HCF.
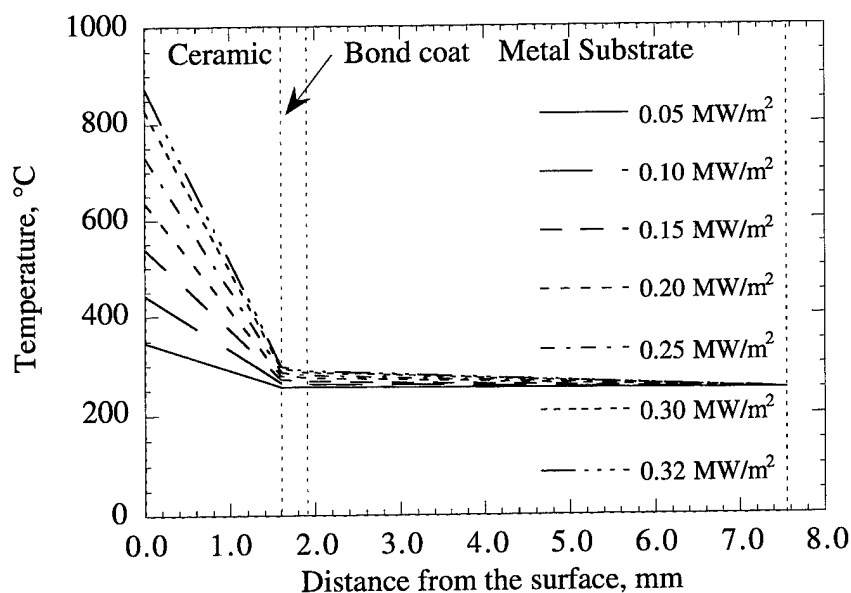
Fig. 5   Temperature distributions in a thermal barrier coating system on an angle iron at steady state heating for various heat fluxes.
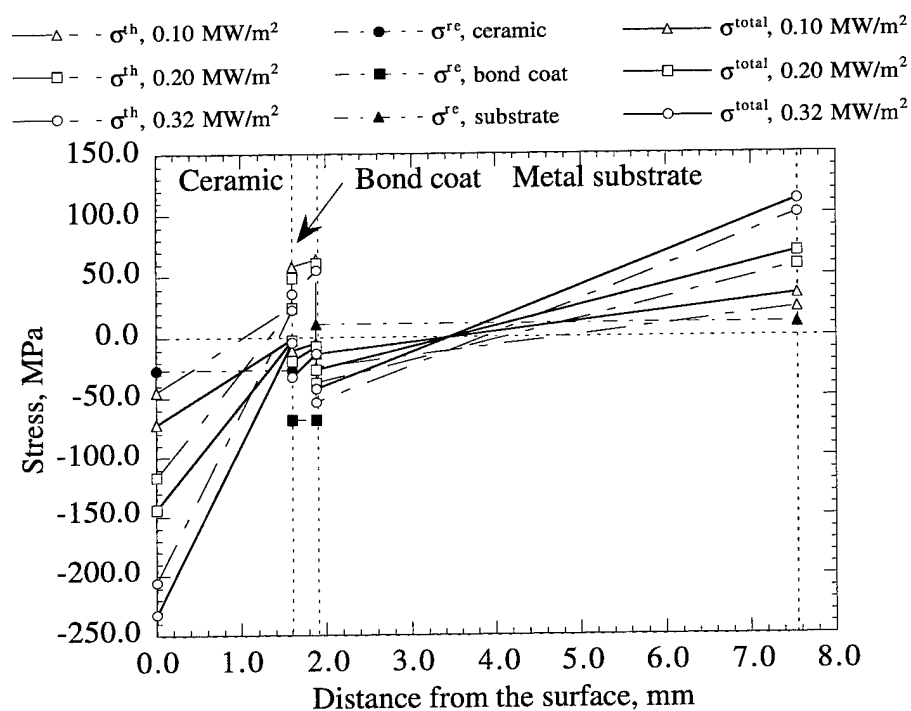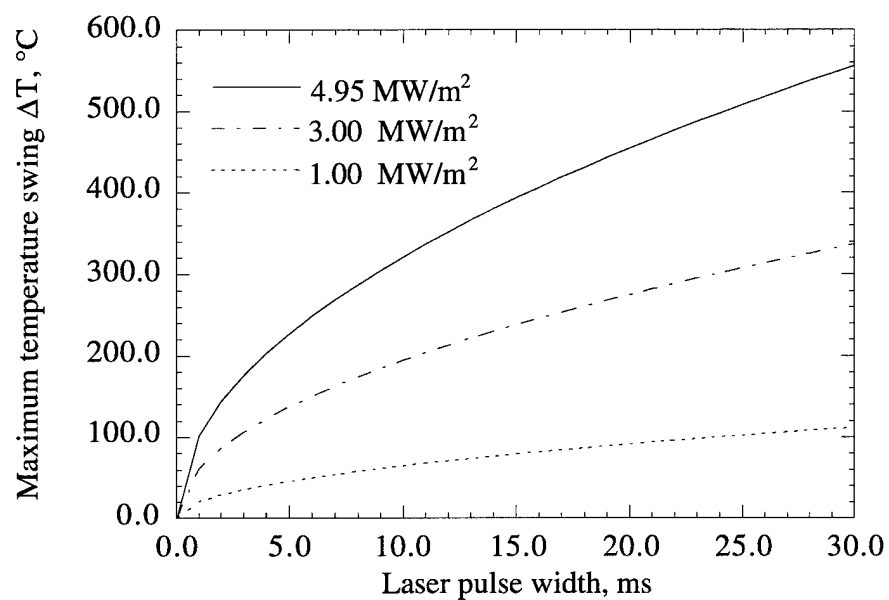

Fig. 6   Stress distributions in a thermal barrier coating system on an angle iron at steady state heating for various heat fluxes.

Fig. 7 Maximum temperature fluctuation, calculated by finite difference analysis, as a function of laser pulse width.
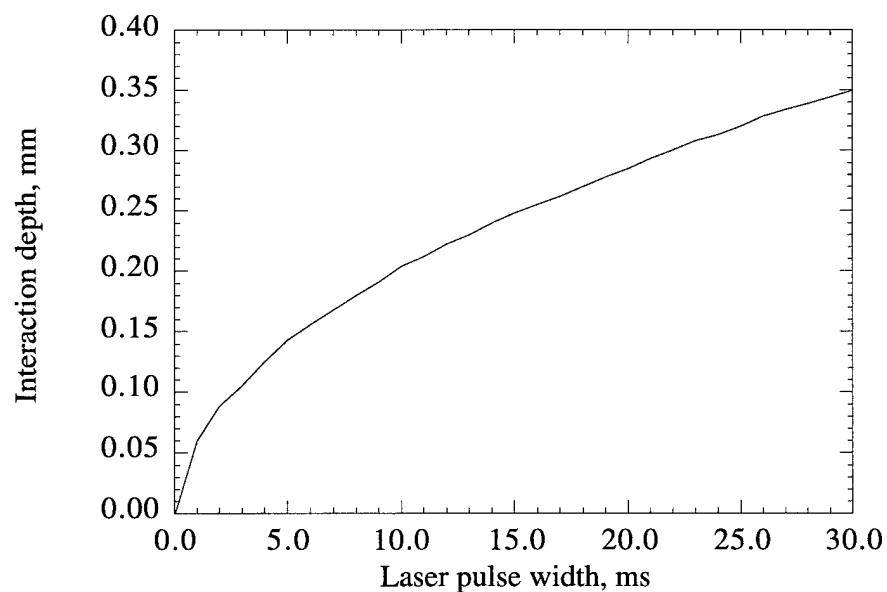
Fig. 8 The relationship between laser interaction depth and laser pulse width. The interaction depth is independent of laser power density.
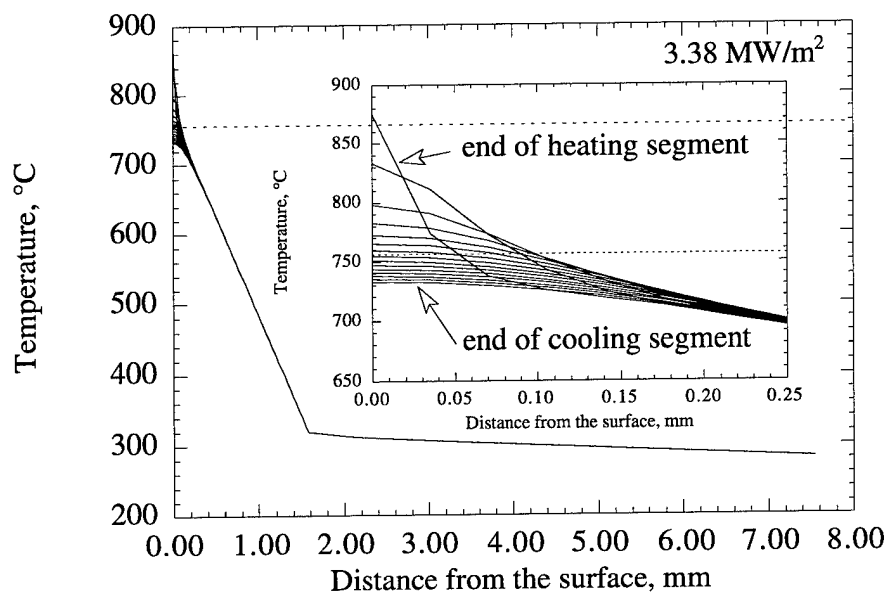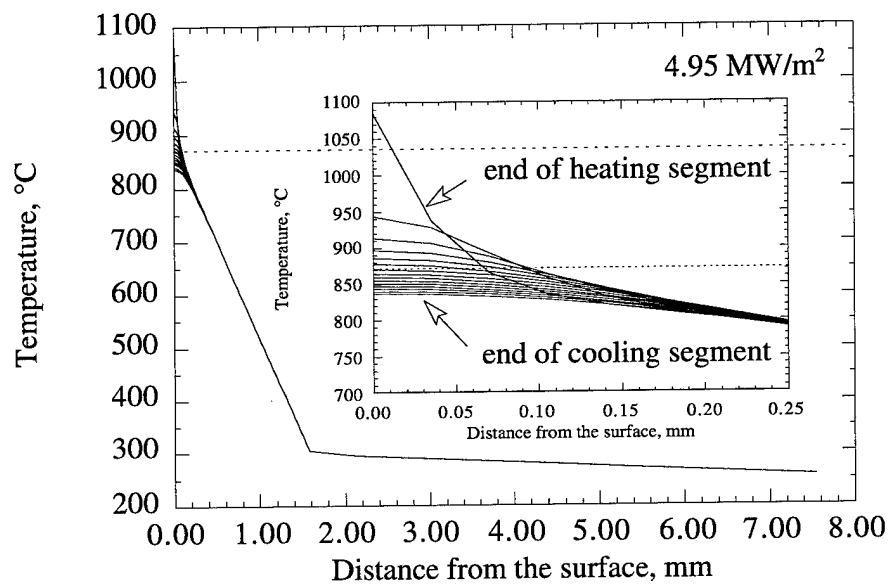
Fig. 9 Predicted temperature profiles generated by pulsed laser heating (pulse width 6 ms). A higher heat flux produces a higher temperature swing and average surface temperature (dashed line represents the average temperature).
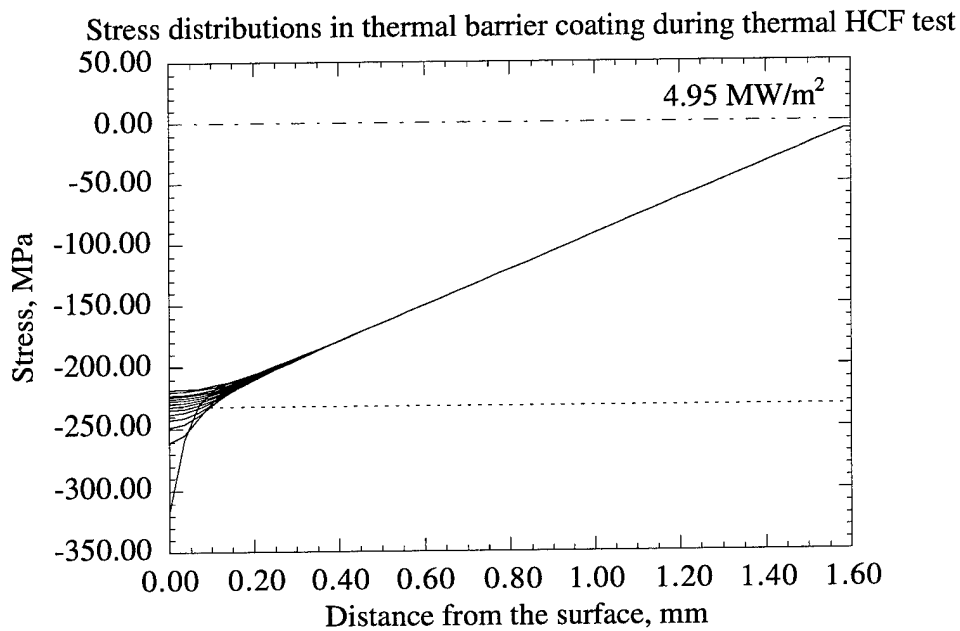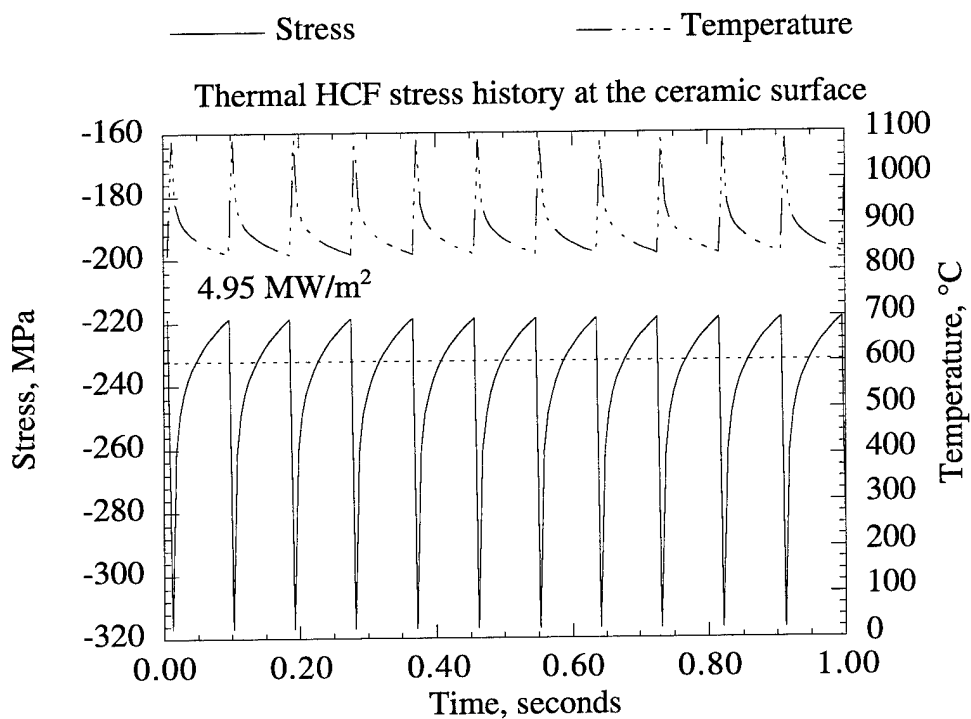
Stress distributions in thermal barrier coating during thermal HCF test

(a)

——————— Stress   ————————— Temperature

Thermal HCF stress history at the ceramic surface
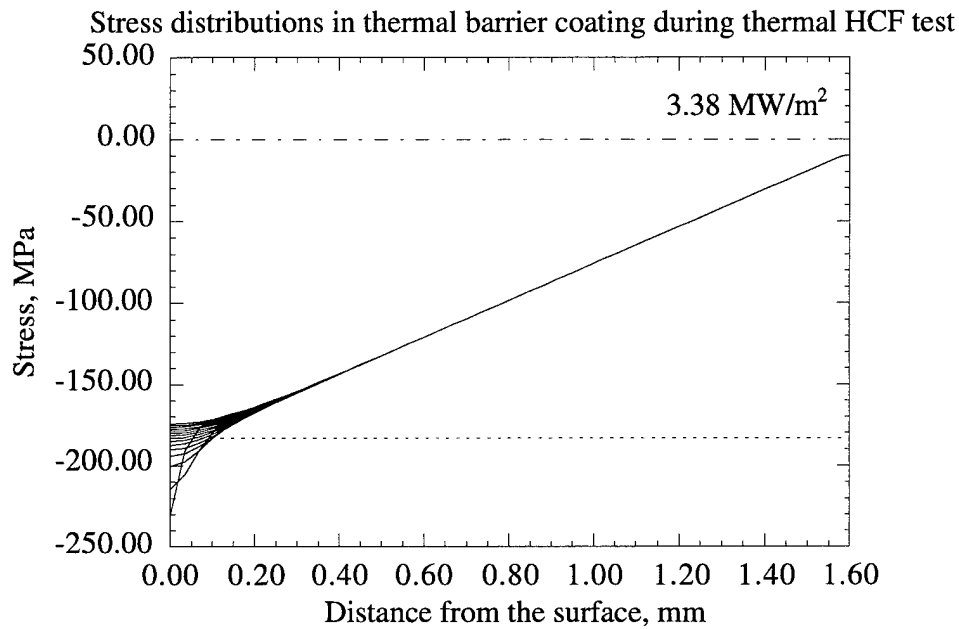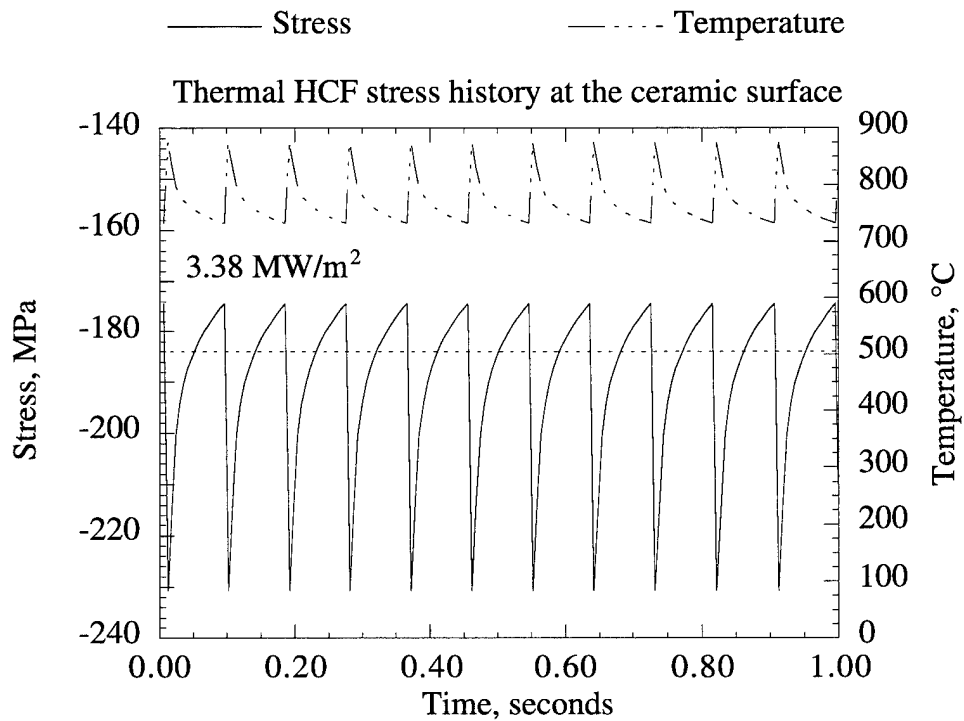
(b)

Fig. 10   Predicted thermal stresses induced by pulsed laser heating. Besides a constant stress gradient generated by the steady state heating, high frequency HCF cyclic stresses are present near the ceramic coating surface. Peak power density 3.38 MW/m^2.

Stress distributions in thermal barrier coating during thermal HCF test

4.95 MW/m²

Stress, MPa

Distance from the surface, mm

(c)

——— Stress   — · · · · - Temperature

Thermal HCF stress history at the ceramic surface

4.95 MW/m²

Stress, MPa

Temperature, °C

Time, seconds

(d)

Fig. 10   Predicted thermal stresses induced by pulsed laser heating. Besides a constant stress gradient generated by the steady state heating, high frequency HCF cyclic stresses are present near the ceramic coating surface (continued). Peak power density 4.95 MW/m².

LCF and HCF Damage on Thermal Barrier Coatings

The surface cracking was observed for all specimens tested under LCF and/or HCF conditions (total heating time up to 256 hours). Compared to the pure LCF tested specimen, the combined LCF and HCF tests produced much higher crack densities, with more complex crack networks on the ceramic surfaces. Examination of surface cracks on the flat specimens shows that the crack density decreases with decreasing laser power density.

The crack patterns on the angle iron and flat specimen surfaces are schematically illustrated in Figure 11. At the angle iron corners, nearly parallel cracks which run across the corners were formed by the laser thermal fatigue tests. In contrast, equiaxial crack networks (mud flat cracks) were generated by the laser beam at the flat specimen surfaces. However, at the edges of the flat specimens, parallel cracks similar to those found on the angle iron corners were observed with crack direction perpendicular to the edges. Compared to pure LCF tests, the combined LCF and HCF initiated more secondary cracks, and micro-spallation at the cracked surfaces. The optical micrographs of the cracked surfaces are shown in Figure 12. The results suggest that much higher surface stresses were induced at the ceramic surface by the pulsed laser HCF component.
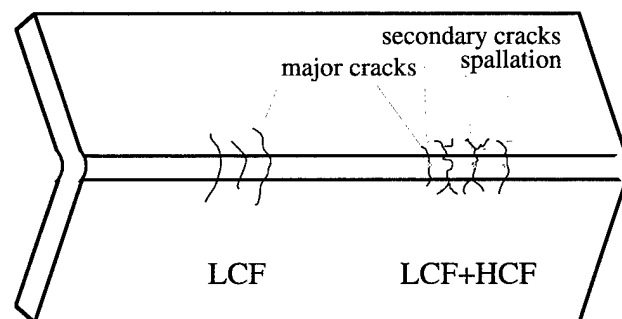
(a) Angle iron specimen
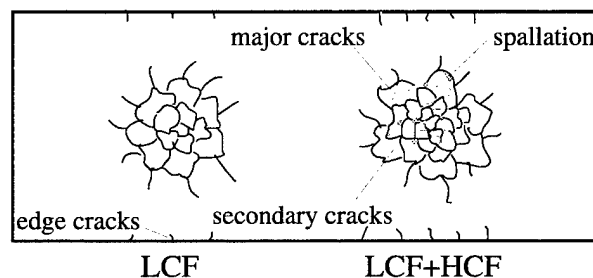
(b) Rectangular flat specimen

Fig. 11   Schematic diagram showing the crack patterns on coating surfaces after laser testing.

Figure 13 shows SEM micrographs of the tested coatings on angle iron specimens. It can be noticed that the pure LCF tested specimen shown in Figure 13 (a) has the most intact coating surface, and the thermal fatigue cracks are relatively regular with well matched crack faces. However, the combined LCF and HCF tests produced more severe coating surface damage. Besides the major thermal fatigue cracks, surface coating micro-spallation, crack branching and loose particles intruding into the cracks are often observed. For all combined LCF and HCF tested specimens, the specimen with the 30 minute heating/5 minute cooling cycles at a lower temperature (850°C) showed the least surface damage. In contrast, the most surface damage was found for the specimen with the 30 minute heating/5 minute cooling cycles at the higher temperature (950°C). In the latter specimen, cracks were branched into multiple crack networks and accompanied with more coating spallation, and the major crack density and the crack width were also significantly higher compared with the lower temperature tested specimens.

DISCUSSION

Ceramic Coating Sintering and Creep at High Temperatures

During thermal fatigue testing, ceramic sintering and creep will occur under the given temperature and stress conditions. Due to the porous and microcracked nature of plasma-sprayed ceramic coatings, the primary creep stage is often observed for these coatings, with the strain rate continuously decreasing with time [15, 16]. This creep behavior is probably related to stress-enhanced ceramic sintering phenomenon, the splat relative sliding, and the stress redistribution around the splats and microcracks. The stress-dependent deformation can result in coating shrinkage and thus stress relaxation at temperature under the compressive thermoelastic stresses. The strain rate $\dot{\varepsilon}_p$ can be generally written as

$$\dot{\varepsilon}_p = A \cdot \exp\left(-\frac{Q}{RT}\right) \cdot \left(\sigma_{th}\right)^n \cdot t^{-s} \tag{2}$$

where A, n and s are constants, Q is activation energy, R is gas constant, σ_{th} is the in-plane compressive thermal stress in the coating, and t is time. The time exponent s is reported to be 0.82 under low stresses (<80 MPa), and to be 0.67 under high stresses (up to 655 MPa) [15, 16]. The creep strain $\varepsilon_p{}^i$ in the ceramic coating can be expressed as

$$\varepsilon_p{}^i = \int_0^{t_i} \dot{\varepsilon}_p(\sigma_{th}, T, t)dt = \int_0^{t_i} A \cdot \exp\left(-\frac{Q}{RT}\right) \cdot \left(\sigma_{th}^0 - \varepsilon_p{}^{i-1} \frac{E_c}{1 - \nu_c}\right)^n \cdot t^{-s} dt \qquad (3)$$

where $\varepsilon_p{}^i$ and $\varepsilon_p{}^{i-1}$ are creep strains at time t_i, and the previous time step t_{i-1}, respectively, σ_{th}^0 is the initial thermal compressive stress in the coating, E_c and ν_c are the elastic modulus and Poisson's ratio of the ceramic coating. The stress relaxation effect on the total creep strain is considered by the $\varepsilon_p{}^{i-1}$ term in Equation (3). Using the literature reported data A, n, s and Q for the plasma-sprayed ceramic coating [15, 16], the creep strains as a function of time can be estimated for a heat flux 0.323 MW/m², as illustrated in Figure 14 (a) and (c). The in-plane stress distribution profiles in the coating, as shown in Figure 14 (b) and (d), indicate that significant stress relaxation will occur, especially at the top half of the coating, because of higher thermal stresses and temperatures at these locations. In addition, the creep strain and thus stress relaxation increase with decreasing the time exponent s. The coating creep and stress relaxation are strongly dependent upon the stress exponent, n, and the activation energy, Q. As illustrated in Figures 14 and 15, with a higher n value and a slightly lower activation energy, more significant stress relaxation will occur in the coating system.

The laser heat flux has a significant effect on coating creep and stress relaxation. As shown in Figure 16, a lower laser heat flux (0.20 MW/m²) will establish a lower surface temperature and a less steep temperature gradient across the coating, therefore, a lower thermal stress will be expected in the coating. As a consequence, total creep strain and stress relaxation will be much less as compared with those in the high heat flux case.
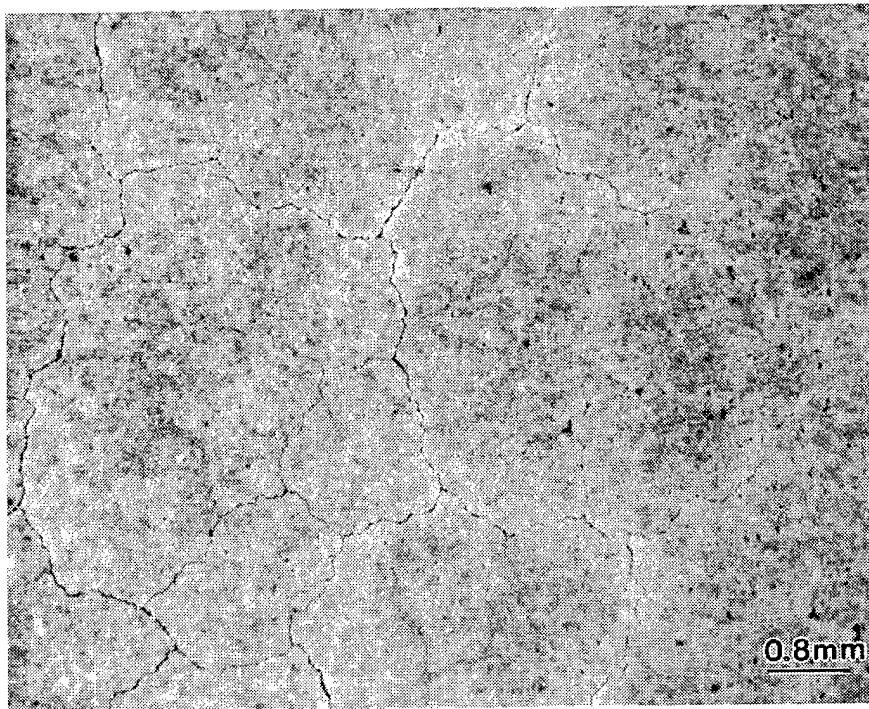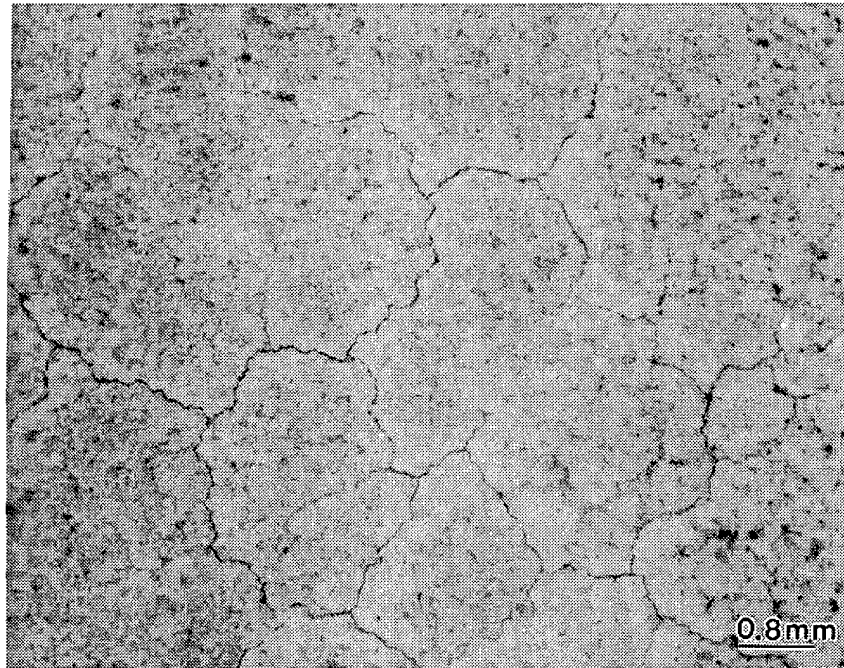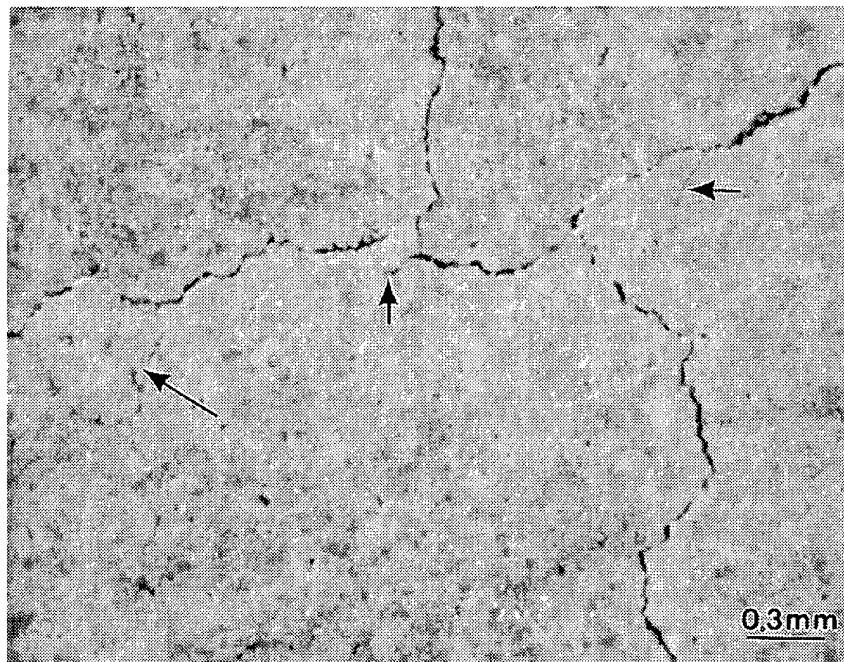
(a)
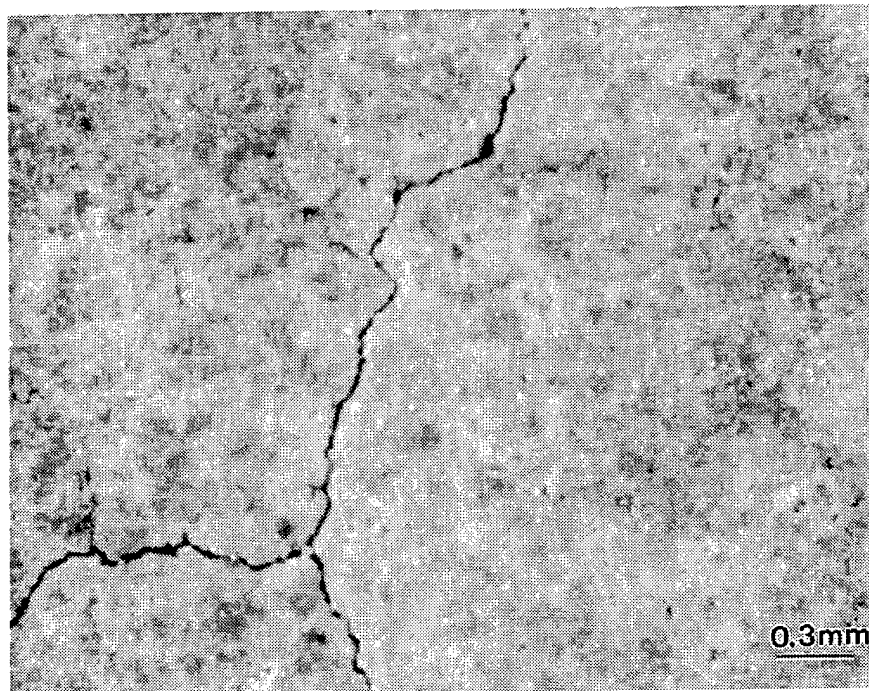
(b)

Fig. 12 Optical micrographs showing the cracked coating surfaces after laser thermal fatigue testing. (a) and (b) The coating surface with pure LCF test;
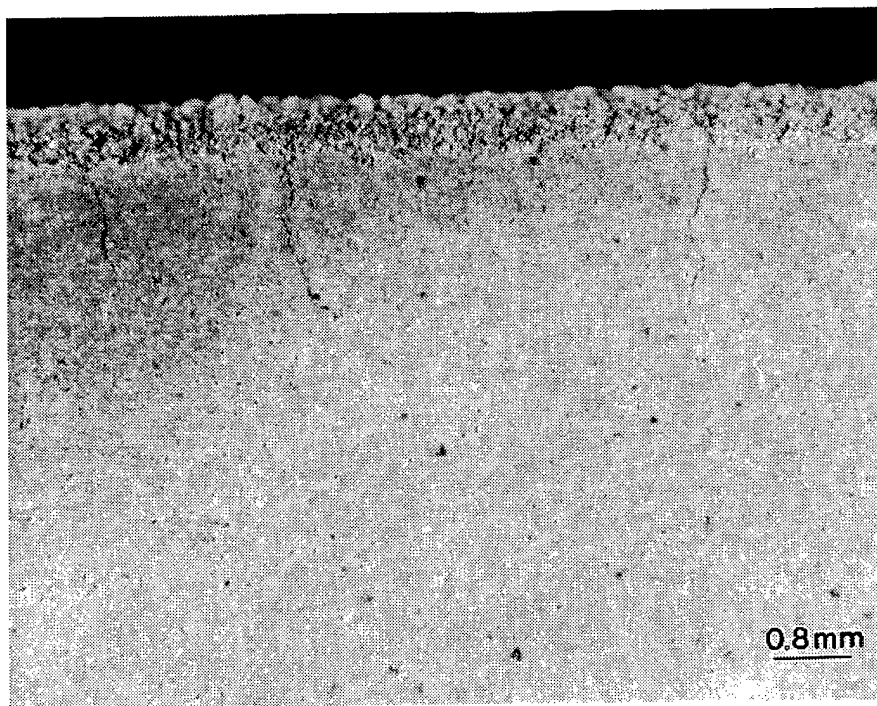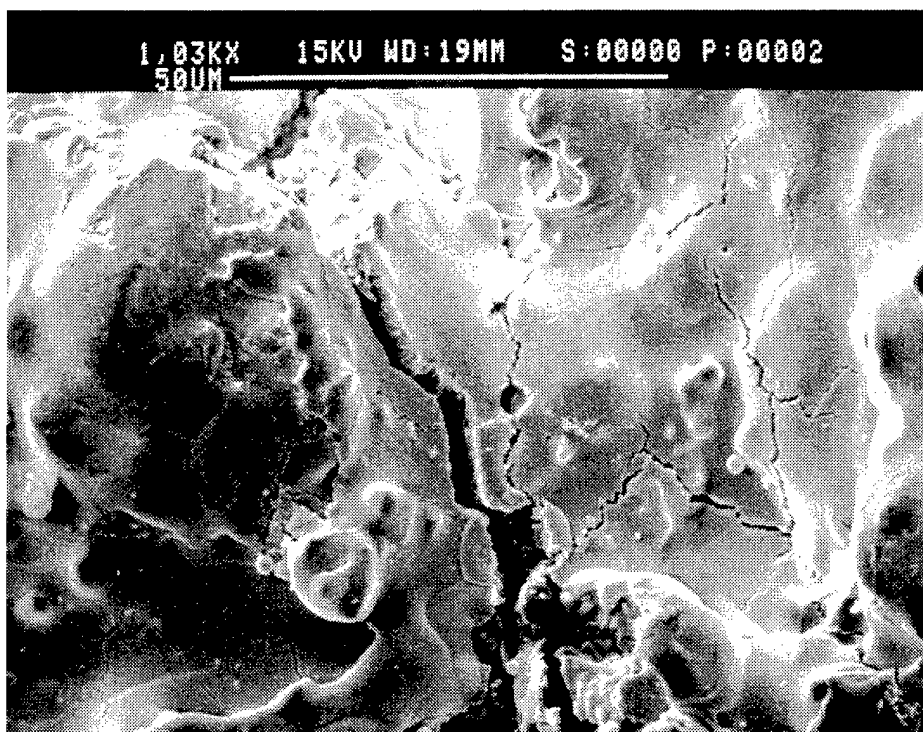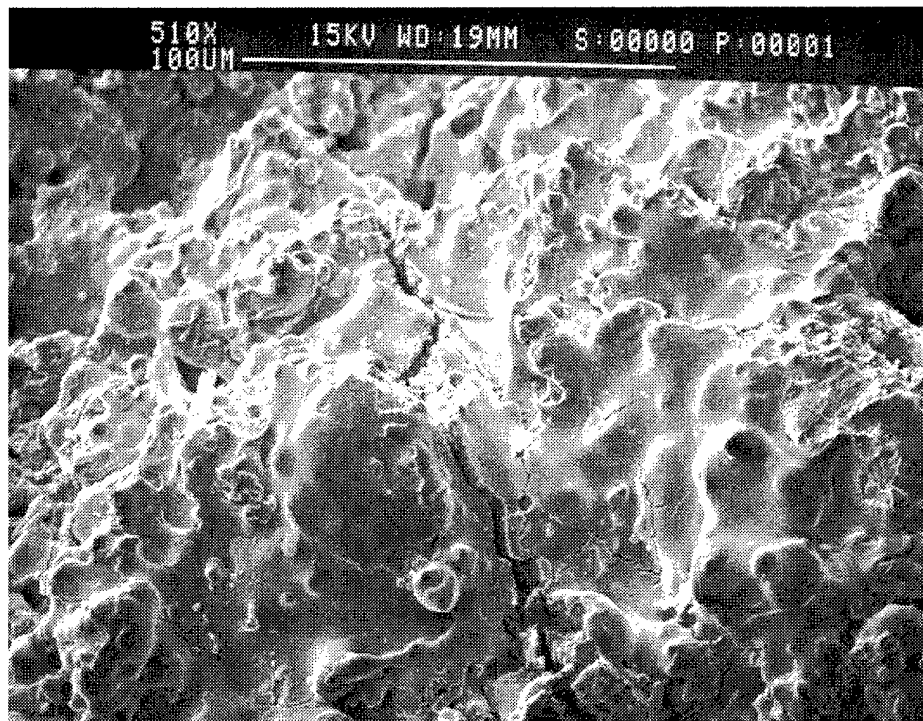
(c)

(d)

Fig. 12 Optical micrographs showing the cracked coating surfaces after laser thermal fatigue testing (continued). (c) and (d) The coating surface with LCF+HCF test (arrows show regions with imminent spalling);
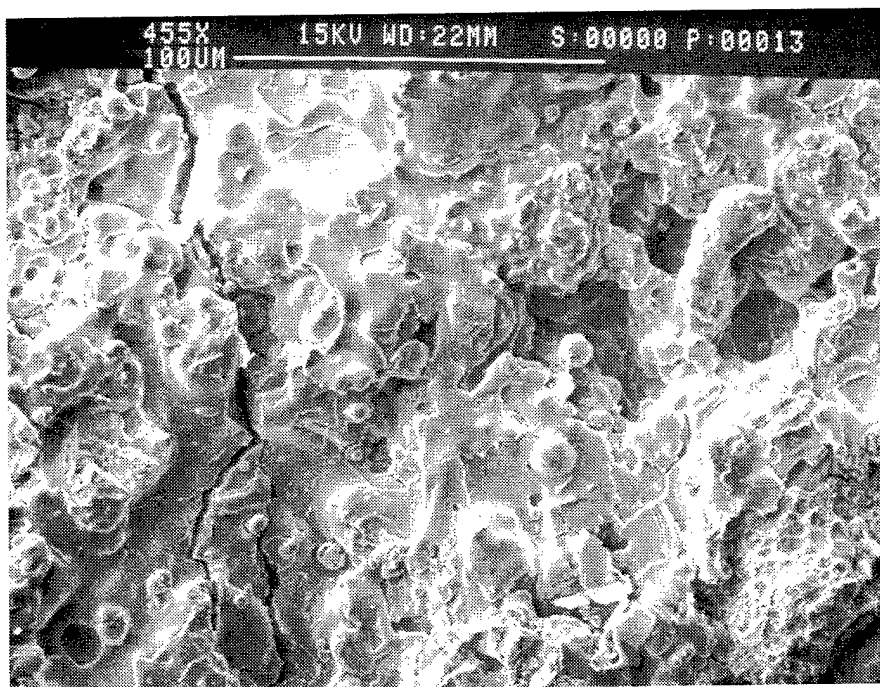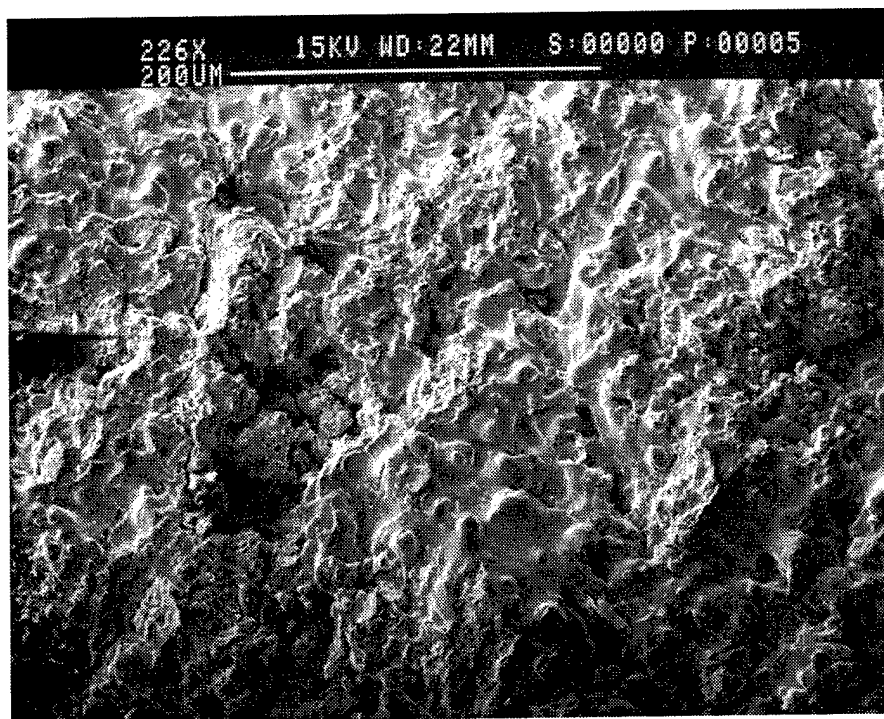
(e)

Fig. 12 Optical micrographs showing the cracked coating surfaces after laser thermal fatigue testing (continued). (e) The coating edge with LCF+HCF test.
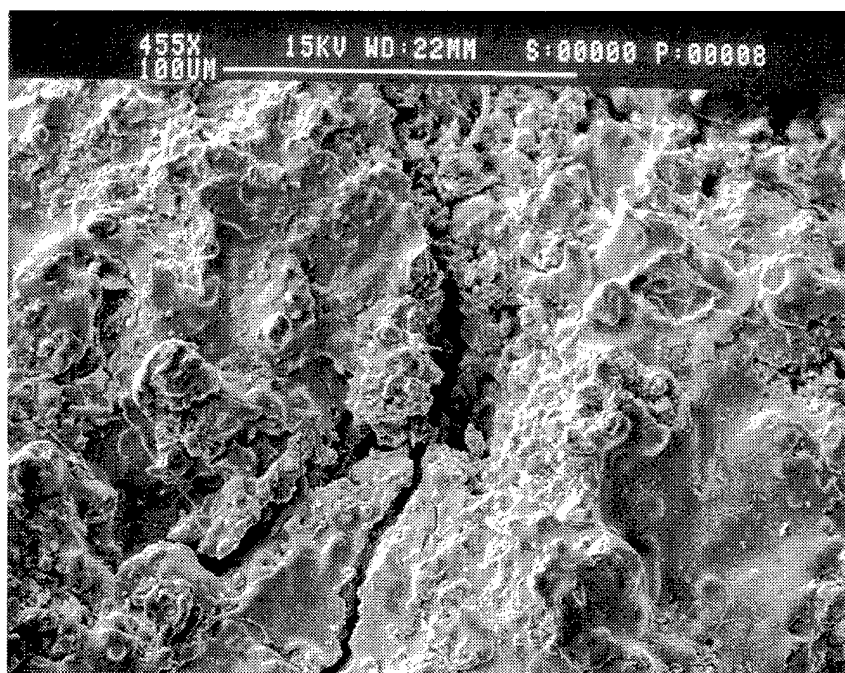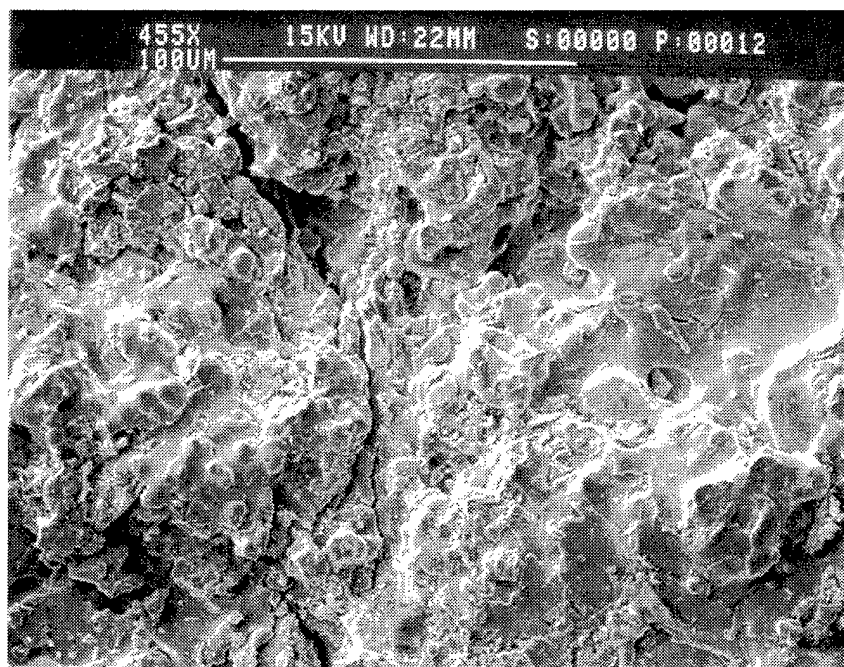
Fig. 13 SEM micrographs showing the coating surface morphologies after laser thermal LCF and HCF testing for angle iron specimens. (a) LCF tested, 5 min. heating/3 min. cooling cycle, center temperature 850°C.
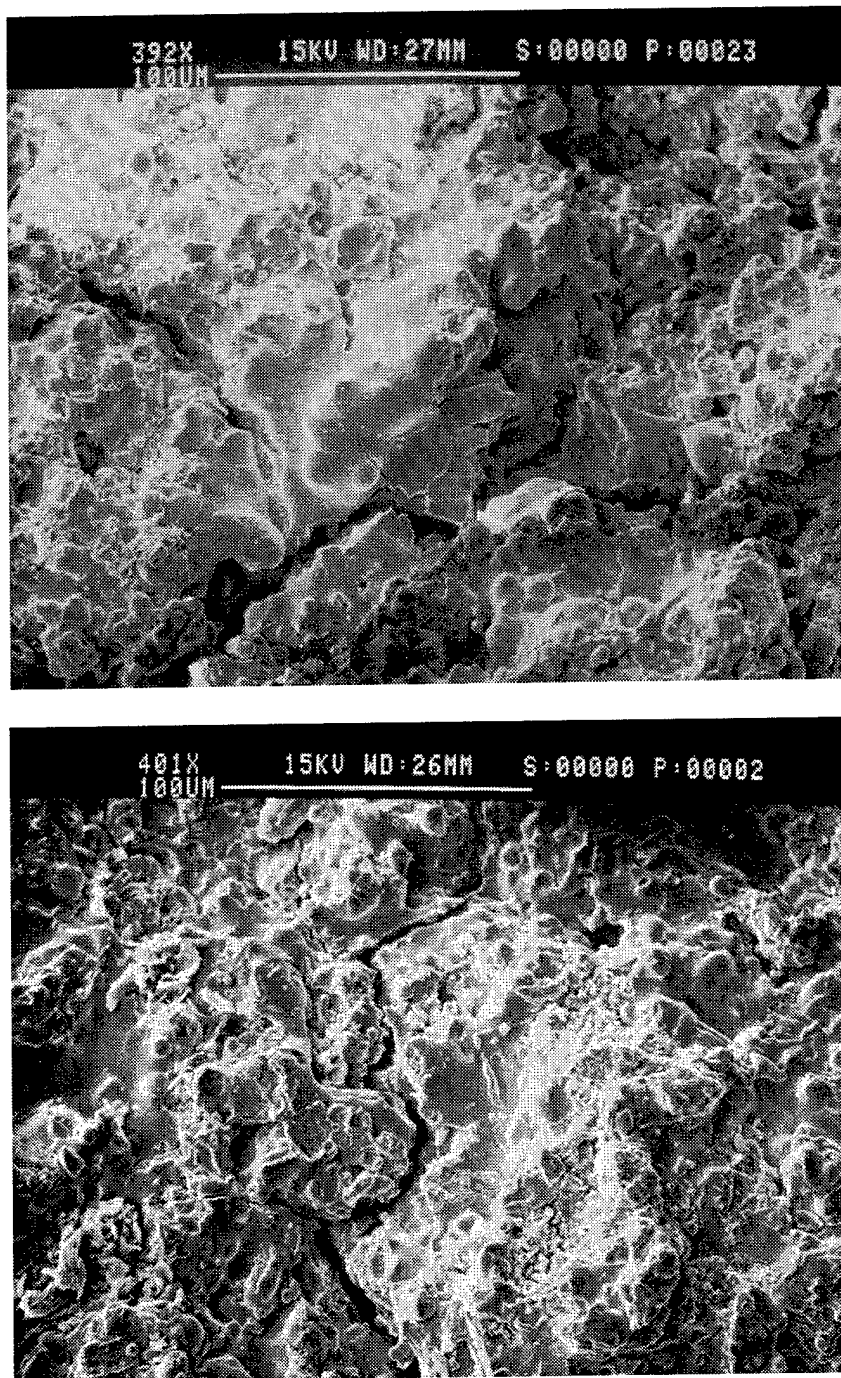
(b)

Fig. 13   SEM micrographs showing the coating surface morphologies after laser thermal LCF and HCF testing for angle iron specimens (continued). (b) LCF+HCF tested, 30 min. heating/5 min. cooling cycle, center temperature 850°C.

(c)

Fig. 13 SEM micrographs showing the coating surface morphologies after laser thermal LCF and HCF testing for angle iron specimens (continued). (c) LCF+HCF tested, 5 min. heating/3 min. cooling cycle, center temperature 850°C.
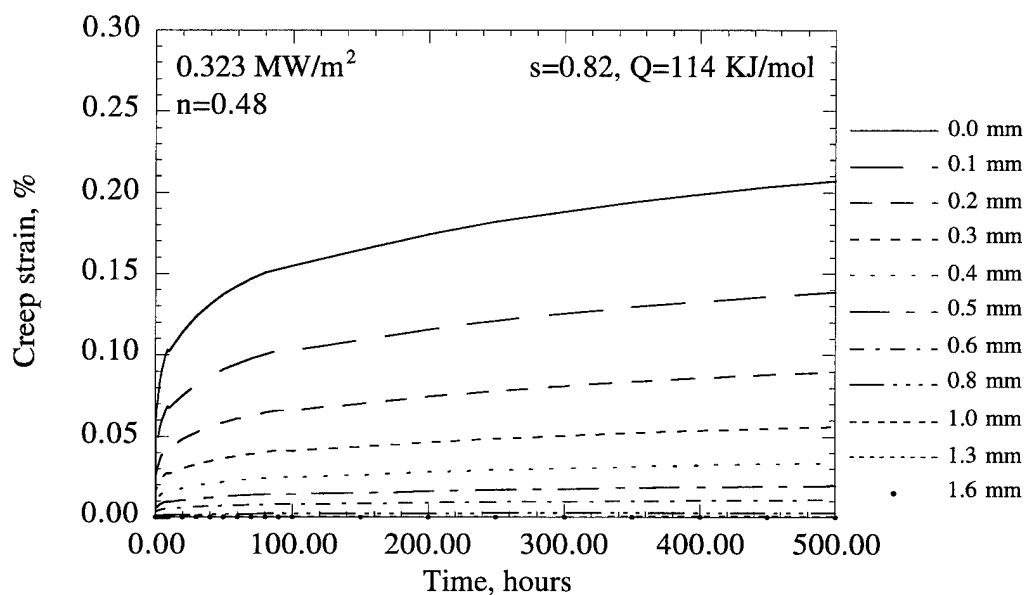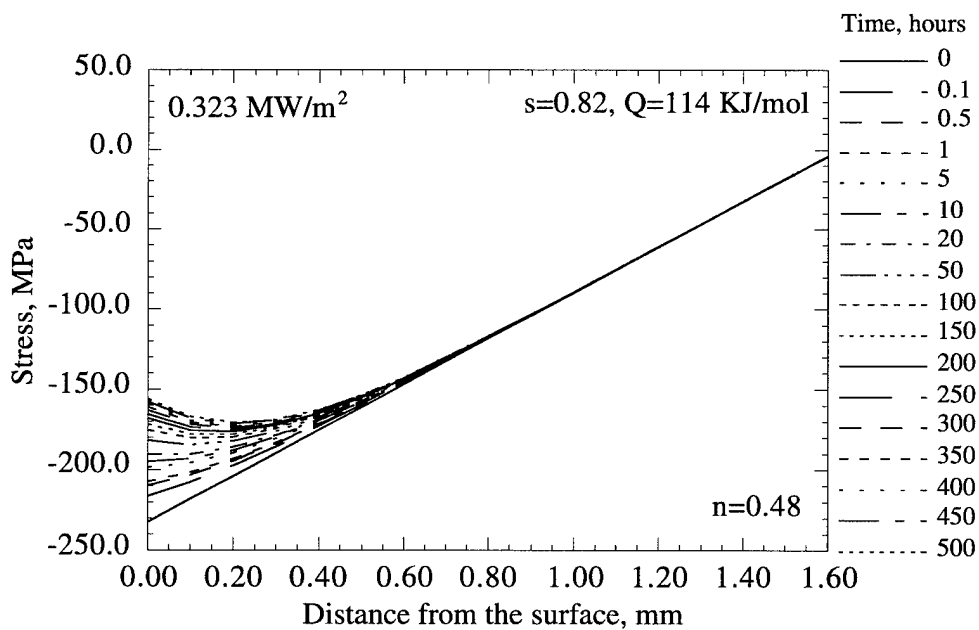
(d)

Fig. 13 SEM micrographs showing the coating surface morphologies after laser thermal LCF and HCF testing for angle iron specimens (continued). (d) LCF+HCF tested, 30 min. heating/6 min. cooling cycle, center temperature 950°C.

Fig. 14 The creep strains and stress relaxation in the ceramic coating as a function of time. The results are estimated from available literature data for the case of heat flux 0.32 MW/m². The total strains and stress relaxation at different layer depths in the ceramic coating increase with the time exponent s. (a) and (b) $s = 0.82$.
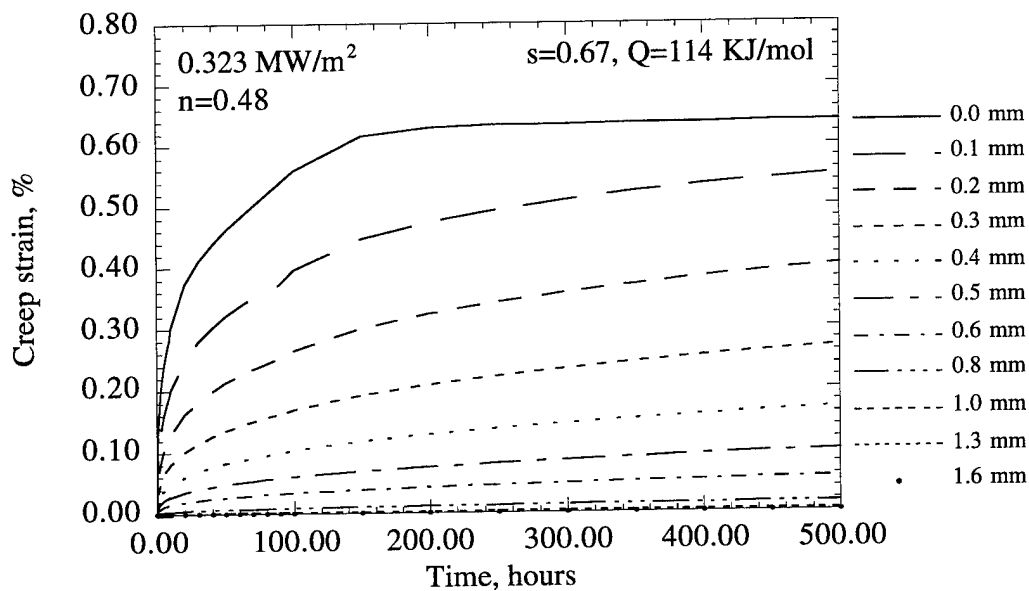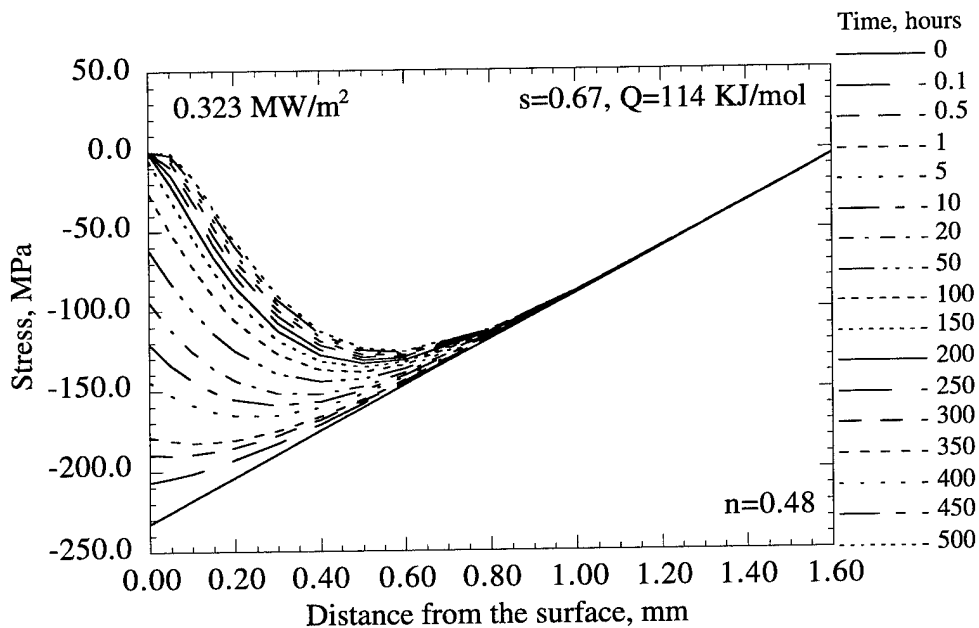
(c)

(d)

Fig. 14   The creep strains and stress relaxation in the ceramic coating as a function of time. The results are estimated from available literature data for the case of heat flux 0.32 MW/m². The total strains and stress relaxation at different layer depths in the ceramic coating increase with the time exponent s. (c) and (d) $s = 0.67$.
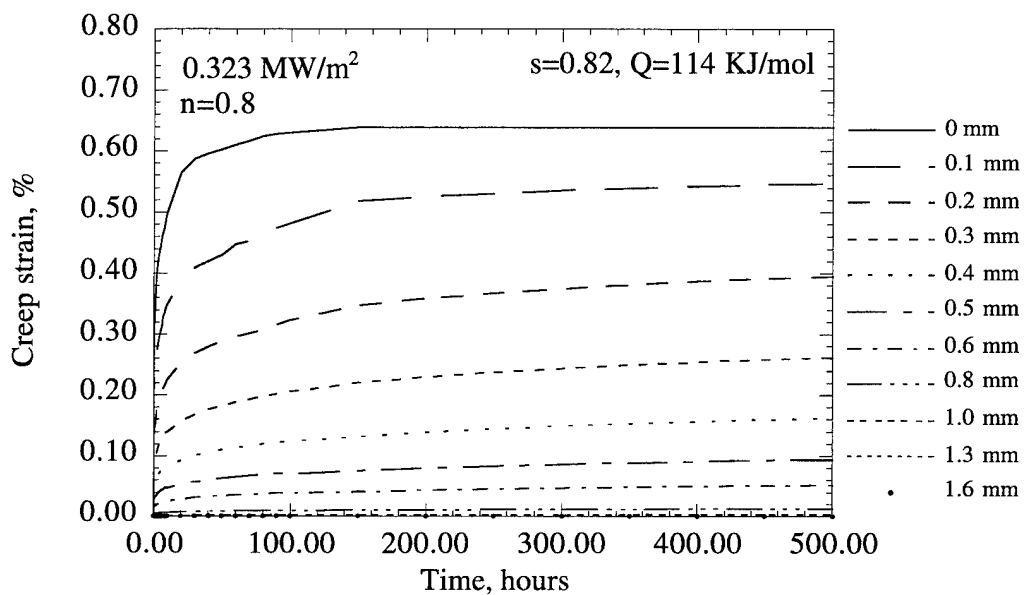
(a)
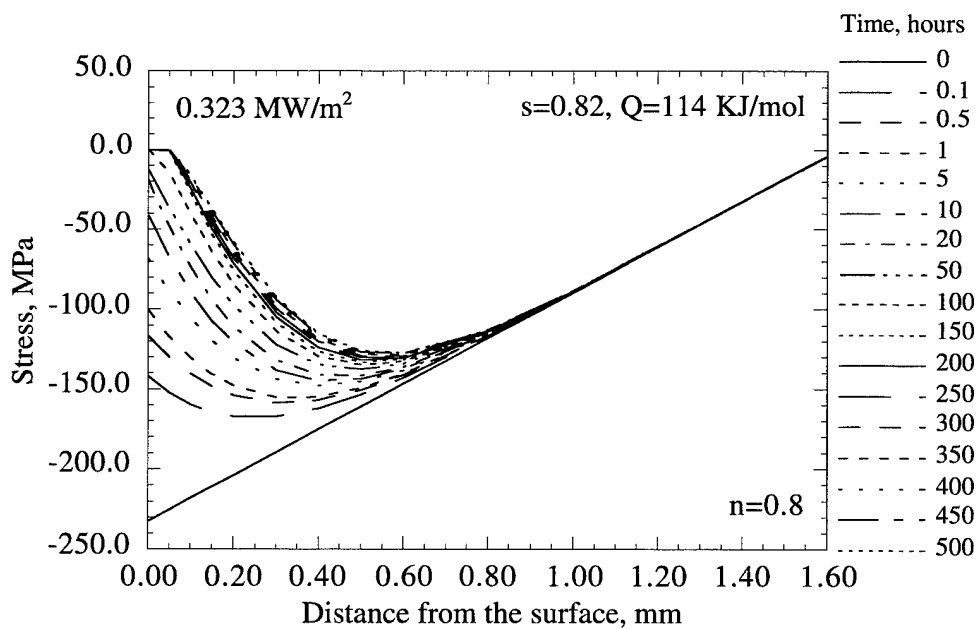
(b)

Fig. 15 The creep strains and stress relaxation in the ceramic coating as a function of time. Compared with Fig. 14, the total creep strains and stress relaxation in the ceramic coating are increased with a higher stress exponent n and a lower activation energy Q. (a) and (b) $n = 0.8$.

(c)

(d)

Fig. 15 The creep strains and stress relaxation in the ceramic coating as a function of time. Compared with Fig. 11, the total creep strains and stress relaxation in the ceramic coating are increased with a higher stress exponent n and a lower activation energy Q. (c) and (d) $Q = 100 KJ / mol$.
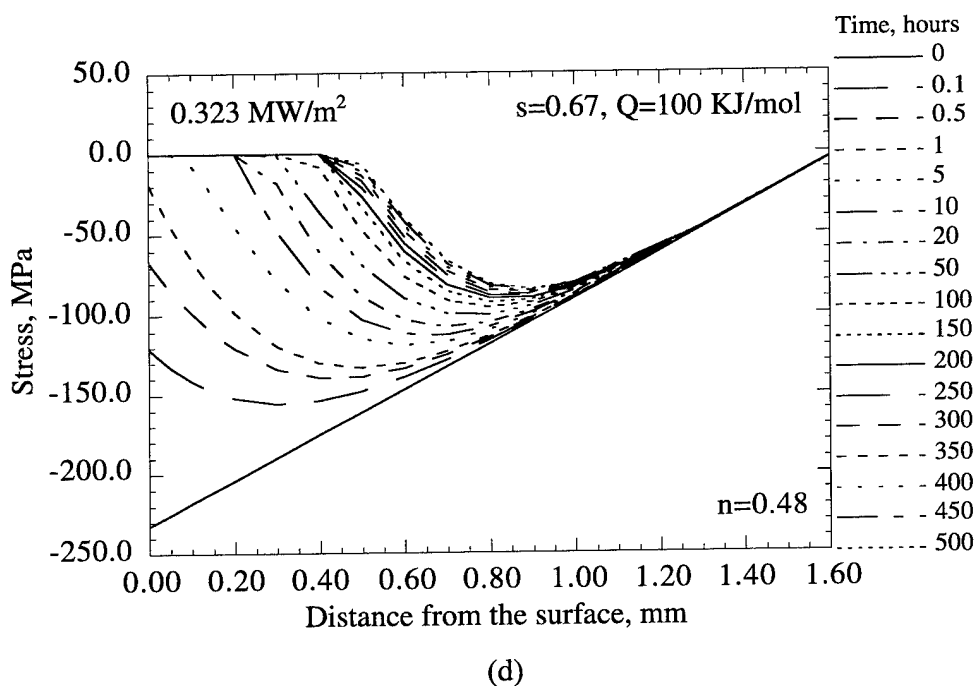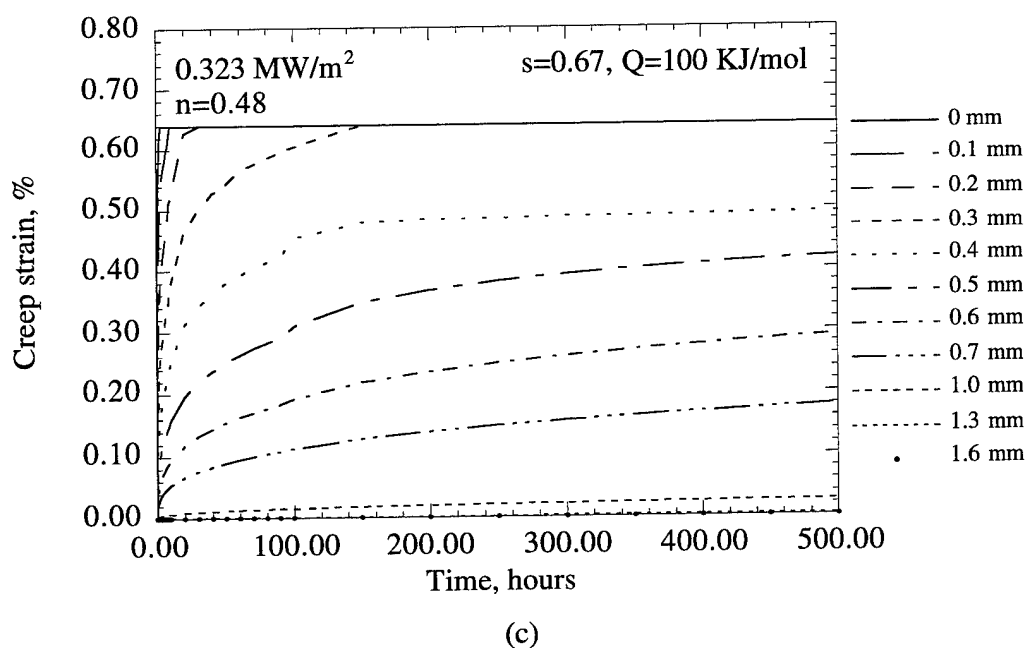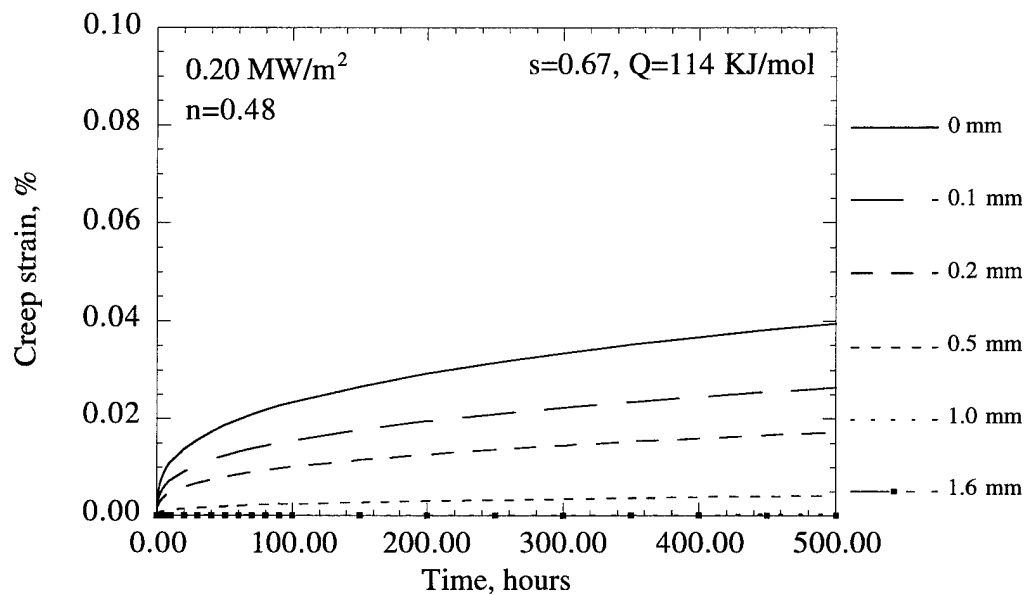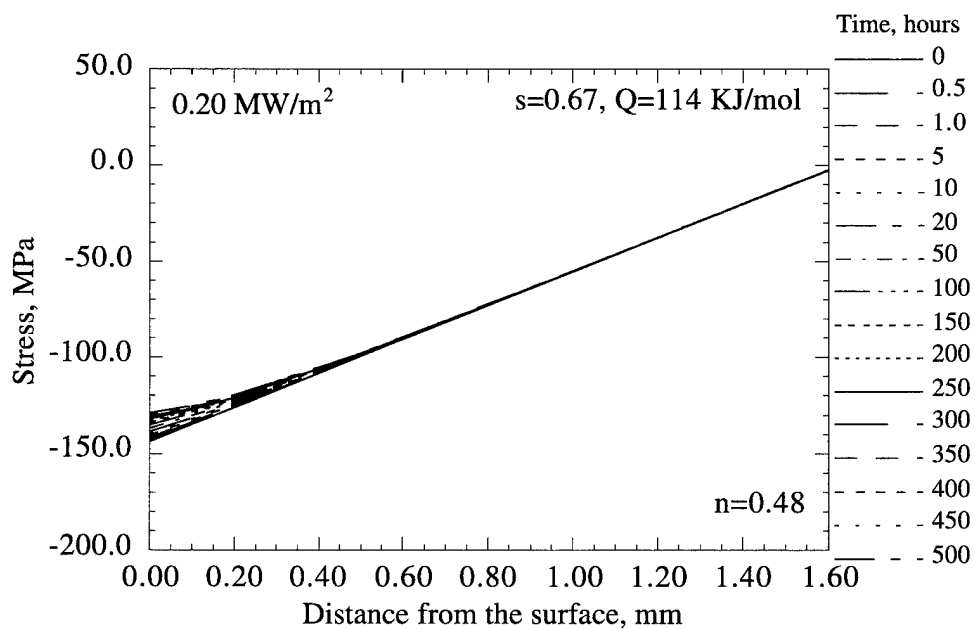
Fig. 16   The creep strains and stress relaxation in the ceramic coating as a function of time
for the case of a lower heat flux 0.2 MW/m².

Crack Initiation During Thermal Fatigue Tests

The plasma sprayed ZrO_2-Y_2O_3 ceramic coatings contain microcrack networks with a typical crack width around 0.5-1 μm after processing. Therefore, initiation of larger cracks at the coating surface during thermal fatigue testing will not be a difficult process. The mechanisms of the crack initiation can be surface tensile stress induced cracking during cooling, and/or HCF peak compressive stress induced cracking at the heating stage. The surface tensile stresses are mainly generated by coating shrinkage after cooling due to the coating sintering and creep at temperatures. The pulsed laser induced temperature swing can generate locally high compressive stresses that could result in the surface coating fracture in a short time period. Since the laser HCF component will promote both the coating surface creep and the coating surface compressive cracking, the accelerated crack initiation and higher surface crack density at the coating surfaces are expected. This has been confirmed by this experiment.

Fatigue Behavior of Thick Thermal Barrier Coatings under Thermal Cyclic Loading

The fatigue crack propagation rates in a ceramic material under cyclic loads can be written as [17-19]

$$\frac{da}{dN} = CK_{max}^m (K_{max} - K_{min})^p = CK_{max}^m \Delta K^p \qquad (4)$$

where C, m and p are material dependent constants, K_{max} and K_{min} are the maximum and minimum stress intensity factors, and ΔK the stress intensity amplitude, of the crack. Under the condition that K_{min} equals zero, Equation (4) can be reduced to the conventional Paris law relationship [20]

$$\frac{da}{dN} = C \Delta K^q \qquad (5)$$

where $q = m + p$. During a superimposed thermal LCF and HCF testing, the surface vertical crack growth can be generally induced by both LCF and HCF components, as illustrated in Figure 17. The crack growth rate with respect to LCF cycle number can thus be expressed as

$$\left(\frac{da}{dN}\right)_{LCF} = C_1 \left(\Delta K_{LCF}\right)^q + \int_0^{N_{HCF}^*} C_2 \left(\Delta K_{HCF}\right)^q dN_{HCF} \qquad (6)$$

where C_1 and C_2 are constants, N_{HCF}^* is the characteristic HCF cycle number, ΔK_{LCF} and ΔK_{HCF} are stress intensity factors of the crack under low cycle and high cycle loads, respectively. The stress intensity factors are functions of crack geometry, crack length and stress magnitudes. It can be seen that the crack propagation rate depends not only on coating properties, but also on LCF and HCF parameters which define the stress states and fatigue mechanisms.
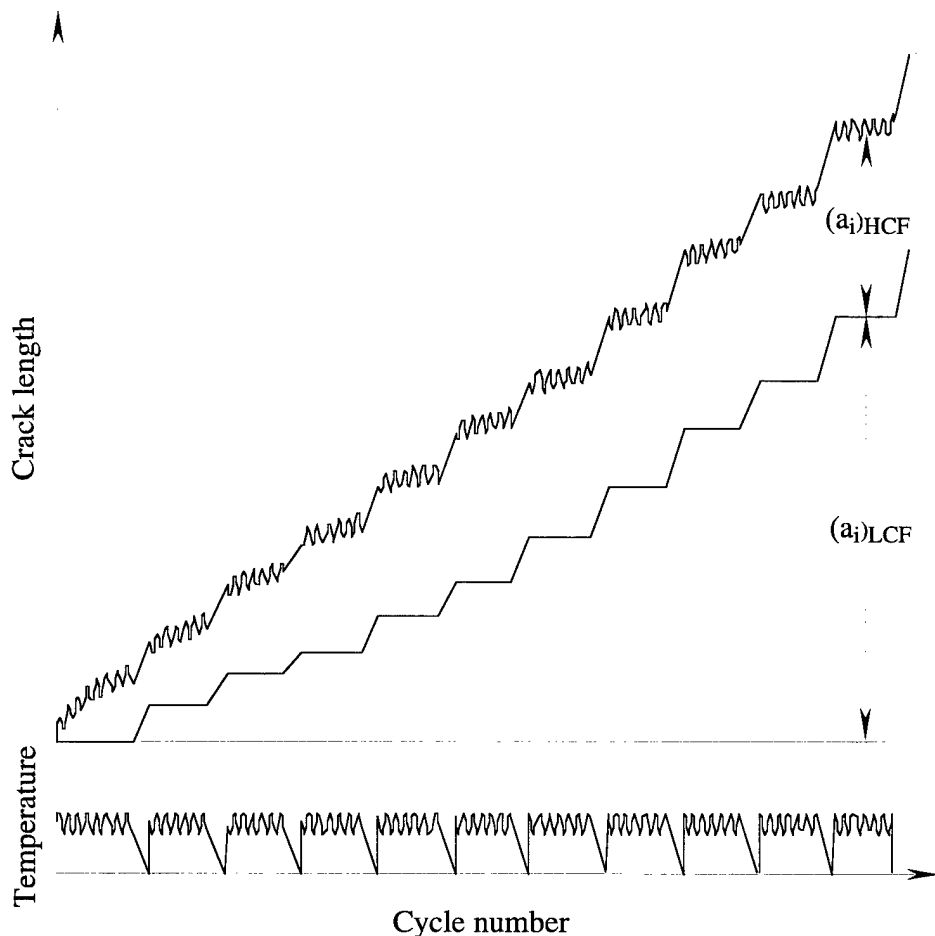
Fig. 17   Schematic diagram showing crack growth resulting from thermal LCF and HCF loads.

Low Cycle Fatigue Mechanism

Under the present test conditions, the oxidation of the bond coat and the substrate is not important because of the low interfacial temperatures and short testing times. Therefore, the low cycle fatigue mechanism is primarily associated with coating sintering and creep at high temperatures. The time and elastic stress dependent, non-elastic strains in

the ceramic coating will lead to a tensile stress state during cooling, as schematically shown in Fig 18. This LCF stress under biaxial condition can be written as

$$\sigma_{LCF} = \int_0^{t_i} \dot{\varepsilon}_p(\sigma_{th}, T, t)dt \cdot \frac{E_c}{1 - \nu_c} \tag{7}$$

where $\dot{\varepsilon}^p(\sigma_{th}, T, t)$ is the strain rate resulting from ceramic sintering or creep, as has been described by Equation (2). The bond coat and metal substrate creep is not considered because of the low temperatures at the interfaces during the thermal fatigue testing. The LCF stresses as a function of time and coating layer depth are illustrated in Figure 19. The mode I stress intensity amplitude for LCF crack growth can be written as

$$\Delta K_{1LCF} = Z \cdot \left[\sigma_{LCF} - \sigma_{th} \right] \cdot \sqrt{\pi a(i)} \tag{8}$$

where Z is a geometry factor associated with the crack configuration. Assuming that the crack does not grow under the compressive thermal stress σ_{th}, the stress intensity will depend primarily on σ_{LCF} and the crack length $a(i)$. Therefore, the LCF crack growth rate will increase with time because of the increased stress σ_{LCF} level and the crack length. However, due to the stress σ_{LCF} distribution profiles in the coating and its interactions with the ceramic/bond coat interface, the crack growth rate becomes more difficult to predict when the crack approaches the interface. Further work is underway to improve the understanding of the crack propagation and interface delamination. From Equation (8), it can also be expected that a faster crack growth rate will result with faster coating sintering and creep rates in the coating.
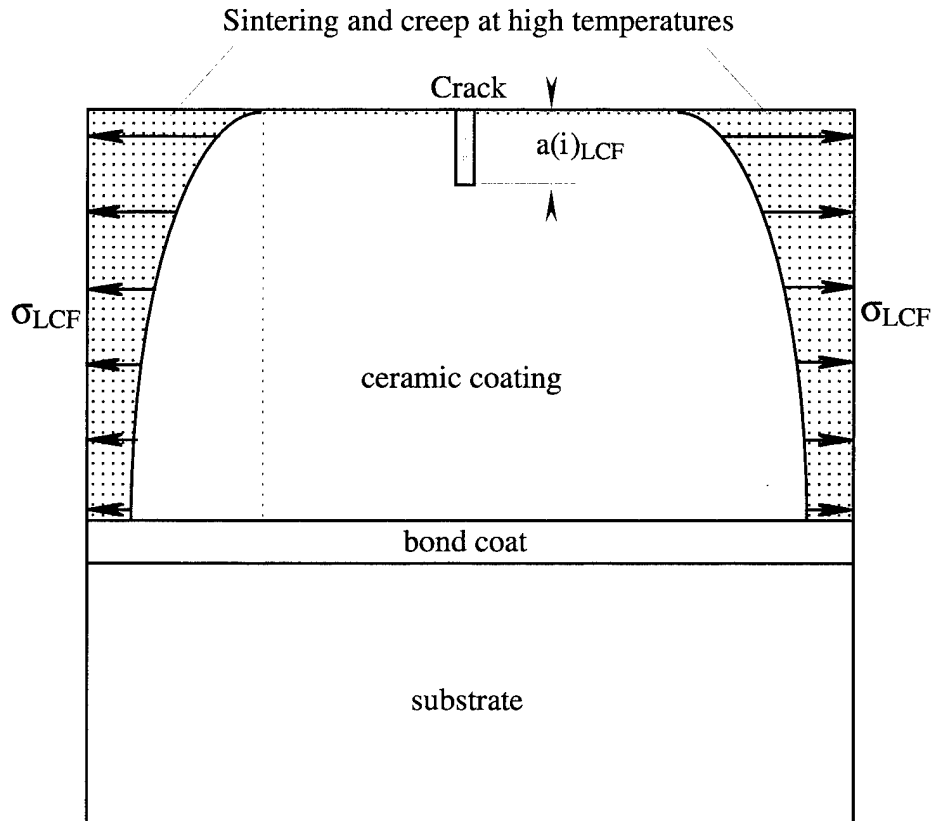
Fig. 18 Ceramic sintering and creep result in non-elastic strains (shown in shadowed area) at temperature, thus generating tensile stresses upon cooling.
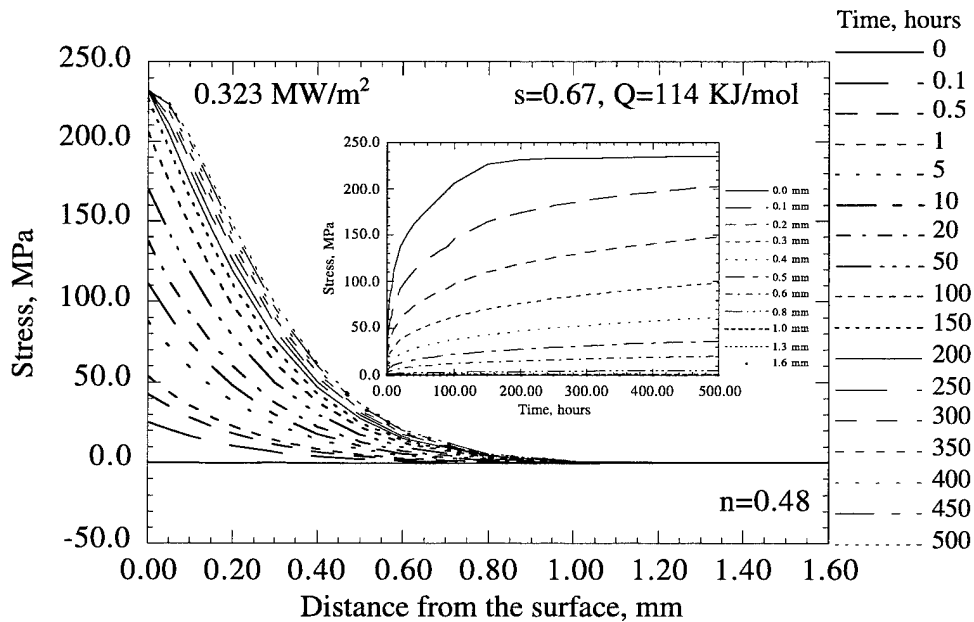

Fig. 19 Tensile stresses are generated in the ceramic coating during cooling as a function of time and coating layer depth. These stresses are considered as a primary mechanism for LCF crack growth.

High Cycle Fatigue Mechanism

The high cycle fatigue is associated with the cyclic stresses originated from the high frequency temperature fluctuation at the ceramic coating surface. Because this temperature swing results in significant thermal strains, considerable stresses will develop at the coating surface. HCF stresses are dynamic in nature, with a very short interaction time; therefore, stress relaxation can be neglected. The HCF stress amplitude is dependent on the temperature swing, and a stress level of 100 MPa can be induced at the surface by a temperature change of 250°C. With a surface crack in the coating, the HCF thermal loads can be equivalently acting on the crack by a wedging process, as schematically illustrated in Figure 20 (a) and (b). This wedging process, which provides an intrinsic mechanism for the HCF phenomenon, can be further enhanced by crack face shifting and spalled particle intruding, as shown in Figure 20 (c) and (d). Since the minimum HCF stress intensity factor equals zero, the net mode I stress intensity amplitude for this case can be expressed as [21]

$$\Delta K_{1HCF} = \frac{2 \cdot P}{\pi} \frac{1 + f(i)}{\sqrt{a(i)^2 - b_i^2}} \sqrt{\pi \cdot a(i)} \tag{9a}$$

and

$$P = \sigma_{HCF} \cdot b_i \tag{9b}$$

where P is a concentrated load per unit thickness acting on the crack, b_i is the load acting distance from the surface which is taken as laser interaction depth in the present study, σ_{HCF} is the HCF stress, $a(i)$ is the crack length at the ith cycle. $f(i)$ is a geometry factor, which can be related to the crack length $a(i)$ and the interaction depth b_i in the following form [21]

$$f(i) = \left[1 - \left(\frac{b_i}{a(i)}\right)^2\right] \cdot \left[0.2945 - 0.3912 \cdot \left(\frac{b_i}{a(i)}\right)^2 + 0.7685 \cdot \left(\frac{b_i}{a(i)}\right)^4\right.$$

$$\left. -0.9942 \cdot \left(\frac{b_i}{a(i)}\right)^6 + 0.5094 \cdot \left(\frac{b_i}{a(i)}\right)^8\right] \tag{10}$$

Note from the above that the stress intensity increases, in a linear manner, with increasing HCF stress σ_{HCF} and, by a more complicated function, with increasing interaction depth b_i. The HCF stress is affected by the temperature swing ΔT, the thermal expansion coefficient α_c and the elastic modulus E_c of the ceramic coating. Figures 21-24

illustrate the relationship between the stress intensity factor and the normalized crack length, with various values of b_i, ΔT, α_c and E_c of the coating. The results show that the stress intensity factor, thus the high cycle fatigue effect, decreases with increasing crack length, but increases with increasing the interaction depth, the temperature swing, the thermal expansion coefficient and Young's modulus of the ceramic coating. It should be noted that, depending on the coating stress state at high temperature, the HCF may affect crack propagation far beyond the laser interaction depth. This has been demonstrated in pure HCF cycling where high temperature swings, and therefore high thermal loads, were generated near the surface of the ceramic coating while the interior of the specimen remained cool [12]. This test condition was shown to cause not only surface crack initiation but also propagation deep into the coating, as shown in Figure 25. In fact, some of the cracks have reached the ceramic/bond coat interface after 5000 cycles when surface temperature swing was 700°C. In another experiment with a lower temperature swing from lower laser energy input, the crack growth was slower.
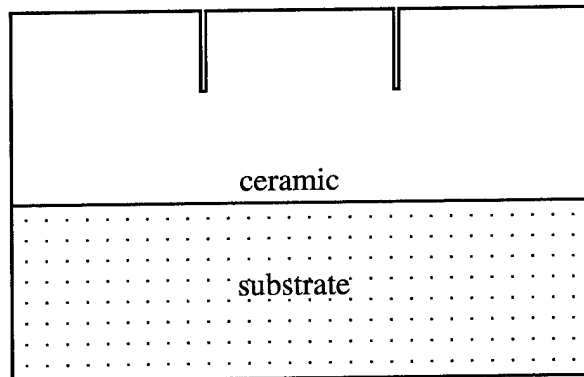
(a) cracks initiated during thermal HCF and LCF tests

HCF interaction layer

σ σ σ σ

a

Δa

ceramic

substrate
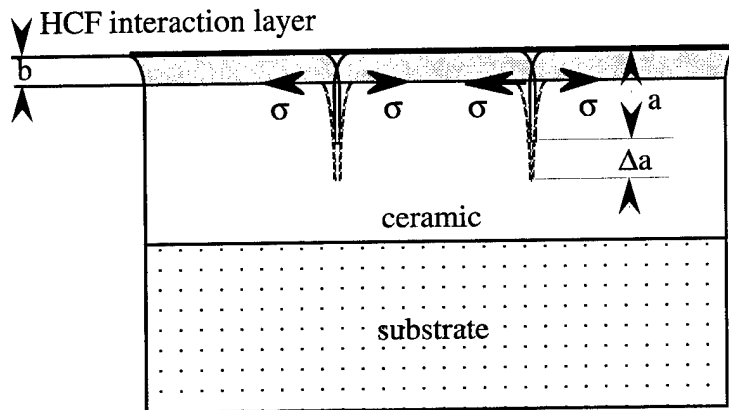
(b) crack growth under HCF conditions by surface wedging mechanism
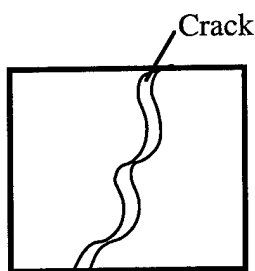
Crack

Crack

(c) enhanced surface wedging damage by surface crack face shifting
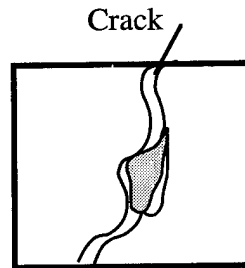
(d) enhanced surface wedging damage by spalled particle intruding

Fig. 20   Schematic diagram illustrating surface wedging mechanism during high cycle fatigue process.

Fig. 21 The relationship between the stress intensity factor amplitude and the laser interacting depth as a function of the normalized crack length.
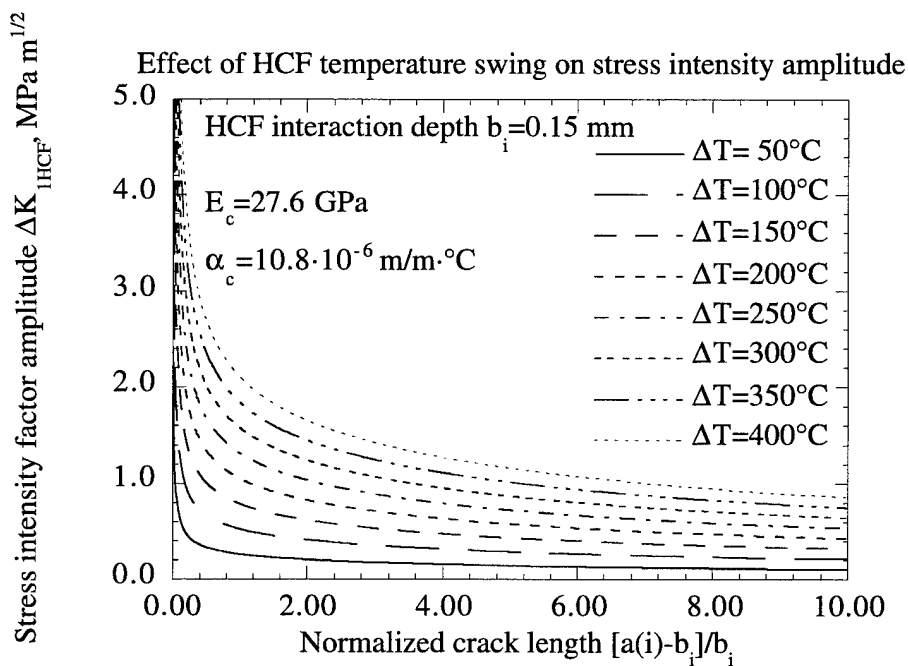
Fig. 22 The relationship between the stress intensity factor amplitude and the temperature swing as a function of the normalized crack length.

Effect of ceramic coating CTE on stress intensity amplitude

HCF temperature swing 250°C
HCF interaction depth b_i=0.15 mm

——— α_c=9·10^{-6} m/m·°C

—— · α_c=10·10^{-6} m/m·°C

— ○— · α_c=10.8·10^{-6} m/m·°C

- - - - - α_c=12·10^{-6} m/m·°C

Stress intensity factor amplitude ΔK_{1HCF}, MPa m$^{1/2}$

Normalized crack length $[a(i)-b_i]/b_i$
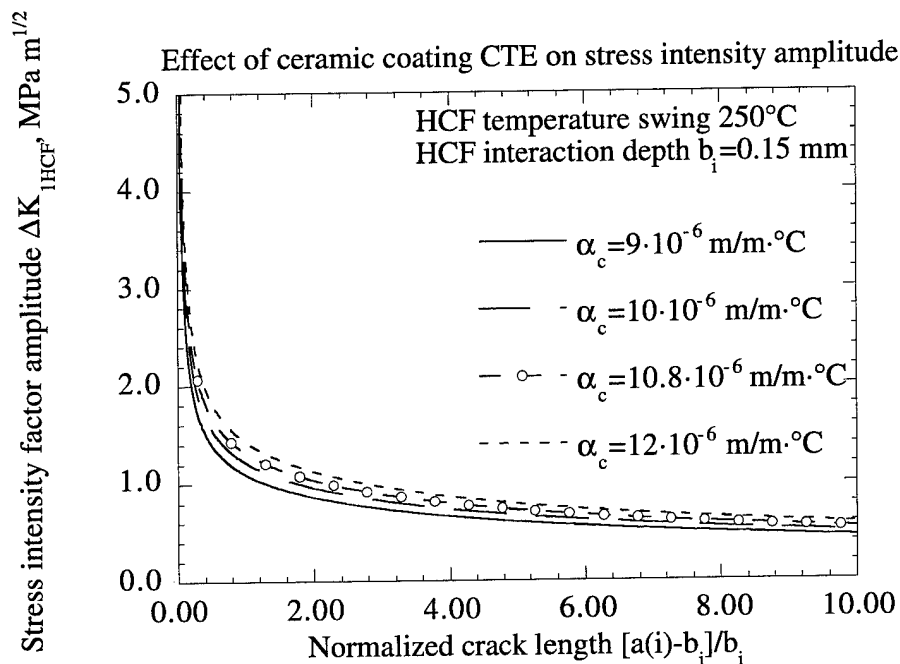
Fig. 23 The relationship between the stress intensity factor amplitude and the thermal expansion coefficient of the coating as a function of the normalized crack length.

Effect of ceramic coating modulus on stress intensity amplitude

HCF temperature swing 250°C
HCF interaction depth b_i=0.15 mm

α_c=10.8·10^{-6} m/m·°C

——— E_c=10GPa

—— · E_c=20GPa

— ○— · E_c=27.6GPa

- - - - - E_c=30GPa

—·—·— E_c=40GPa

········ E_c=50GPa

—··—·· E_c=60GPa

Stress intensity factor amplitude ΔK_{1HCF}, MPa m$^{1/2}$
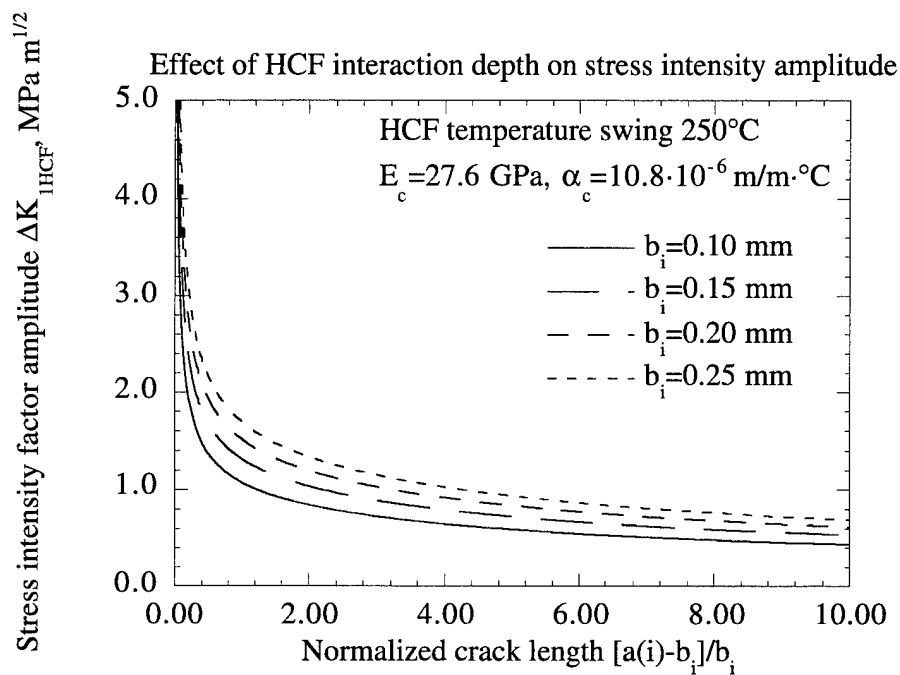
Normalized crack length $[a(i)-b_i]/b_i$
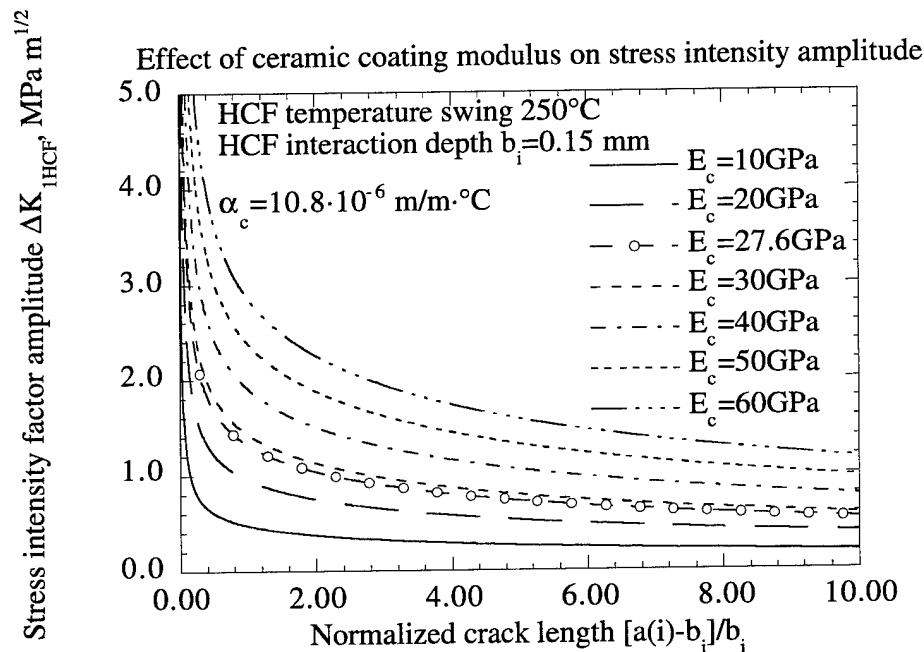
Fig. 24 The relationship between the stress intensity factor amplitude and the elastic modulus of the coating as a function of the normalized crack length.
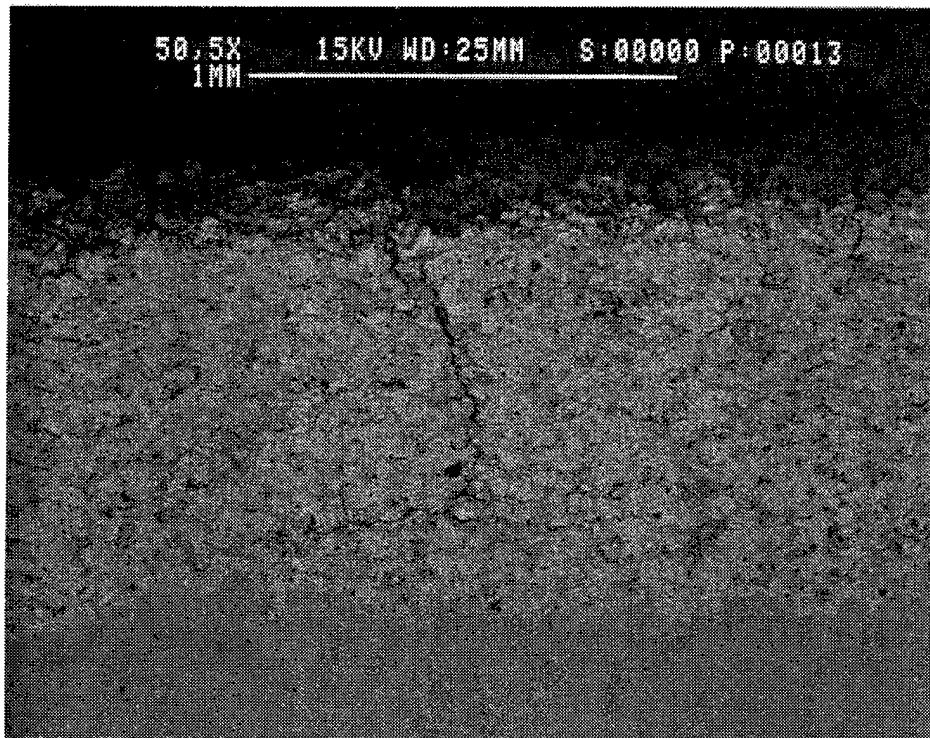
40

Fig. 25 A surface crack propagated deeply into the ceramic coating after 5000
thermal shock cycles at a temperature swing of 700°C. Each laser pulse
heating and cooling cycle consisted of 0.1 second heating and 60 second
cooling, respectively with interaction depth about 0.3 mm.

The Interactions between LCF and HCF Crack Growth

Strong interactions between LCF and HCF have been confirmed by the preliminary experiments. More severe coating damage has been observed for the combined LCF and HCF tests compared to the pure LCF test. The higher crack density and wider crack width observed in the specimens with the higher test temperature suggest that significant coating sintering and creep are detrimental to the coating fatigue resistance. Higher heat flux near the beam center, as imposed by the spatial energy distribution of the Gaussian laser beam, resulted in increased surface cracking and spallation. This result can be expected because a higher heat flux will lead to not only a higher surface temperature and temperature gradient across the coating (generating more significant stress relaxation at temperature and thus more severe LCF damage after cooling), but also a greater temperature swing that enhances HCF failure. It seems to be true that both LCF and HCF are affected by the coating system configurations. In one dimensional coating systems such as angle iron corners and specimen edges, the cracking is less likely to occur in the less constrained direction, which is perpendicular to the one dimensional line direction. This result can be explained by considering that both the LCF and HCF stresses would be much lower in the less constrained direction. This implies that if a perfect bond coat strain isolation can be achieved, the coating fatigue resistance could be greatly improved. Further studies are required to obtain a better understanding of this phenomenon.

The interactions between LCF and HCF lead to an earlier failure of the coating. The high cycle fatigue component promotes surface crack initiation and increases surface crack densities. This causes fast initial crack propagation near the coating surface according to the surface wedging mechanism, because of the extremely high stress intensity values at the initial stage. The longer cracks then increase the subsequent LCF stress intensity amplitudes, thus leading to a faster crack growth rate under the LCF mechanism. The LCF component will accelerate the subsequent HCF crack growth at high temperatures by predominantly two mechanisms. First, stress relaxation at high temperatures, which results from coating sintering and creep under LCF cycling, as well as from LCF induced crack formation and propagation, can significantly reduce the effective compressive stresses in the coating. The HCF crack growth will be facilitated by this process. Second, the coating surface sintering under LCF cycles could considerably increase the coating elastic modulus. A higher coating modulus will lead to higher HCF stresses, and thus enhance the HCF crack growth.

SUMMARY

The present analysis presents a detailed explanation of the processes occurring when thick TBCs are subjected to combined thermal low cycle and high cycle fatigue. This work also provides a framework for developing strategies to manage ceramic layer sintering and creep, thermal expansion mismatch, and other characteristics of the coating system. For example, since ceramic sintering and creep are detrimental to the coating system, creep resistant coatings, especially near the surface region, would be expected to improve the durability of the system. In addition, since it is well known that LCF behavior is closely related to the thermal expansion mismatch, good strain isolation provided by well-structured and compliant bond coats would further improve the fatigue resistance. The HCF resistance could be effectively achieved by high compressive stresses in the coating. A high toughness top surface layer with low modulus and thermal expansion coefficient would also improve the HCF fatigue life. The relative importance of LCF and HCF crack growth and its correlation with coating stress states, creep behavior and bond coat properties need to be carefully investigated.

CONCLUSIONS

1.   Strong interactions between LCF and HCF have been observed in preliminary experiments. The combined LCF and HCF tests induced more severe coating damage compared to the pure LCF test. Significant coating sintering and creep, which are confirmed to accelerate both the LCF and HCF failure by experiments, are detrimental to the coating fatigue resistance.

2.   In the absence of severe interfacial oxidation, the LCF mechanism is closely related to coating sintering and creep phenomena at high temperatures. The stress relaxation, at temperature, induces tensile stresses in the coating after cooling. However, the HCF mechanism is associated with the surface wedging process. The HCF damaging effect will increase with the heat flux, thus the temperature swing, the thermal expansion coefficient and the elastic modulus of the ceramic coating, as well as the HCF interaction depth.

ACKNOWLEDGMENT

REFERENCES

[1]   Yonushonis, T. M., *"Thick Thermal Barrier Coatings for Diesel Components"*, *NASA CR-187111*, August 1991.

[2]   Beardsley, M. B. and Larson, H. J., *"Thick Thermal Barrier Coatings for Diesel Components"*, *DOE/NASA/0332-1, NASA CR - 190759*, 1992.

[3]   Miller, R. A., *"Assessment of Fundamental Materials Needs for Thick Thermal Barrier Coatings for Truck Diesel Engines"*, *NASA TM-103130, DOE/NASA/21794-1*, May,1990.

[4]   Morel, T., *"Analysis of Heat Transfer in LHR Engines: A. Methodology, Validation, Applications; B. Translucence Effects in Ceramics"*, in *Proceedings of the 1987 Coatings for Advanced Heat Engines Workshop* (eds. Fairbanks, J.), II17-II28, Castine, Maine, July 27-30, 1987.

[5]   Dickey, D., Vinyard, S., Callahan, T. and Keribar, R., *"The Effect of Insulated Diesel Surfaces on Performance, Emissions and Combustion"*, in *Proceedings of the Twenty-Fifth Automotive Technology Development Contractors' Coordination Meeting* , 49-56, **P209**, Dearborn, Michigan, October 26-29, 1988.

[6]   Zhu, D. and Miller, R. A., *"Evaluation of Oxidation Damage in Thermal Barrier Coating Systems"*, *NASA TM107360, Army Research Laboratory TR ARL-TR-1254*, November 1996. Also in *"Fundamental Aspects of High Temperature Corrosion"* (eds. Shores, D. A., Rapp, R. A. and Hou, P. Y), 289-307, The Electrochemical Society, Inc., Pennington, New Jersey, 1997.

[7]   Zhu, D. and Miller, R. A., "*On Delamination Mechanisms of Thick Thermal Barrier Coating Systems under Thermal Fatigue Conditions*", in preparation, 1997.

[8]   Takeuchi, Y. R. and Kokini, K., "*Thermal Fracture of Multilayer Ceramic Thermal Barrier Coatings*", Journal of Engineering for Gas Turbines and Power, **116**, 266-271, 1994.

[9]   Kokini, K., Choules, D. B. and Takeuchi, Y., "*Thermal Fracture Mechanisms in Ceramic Thermal Barrier Coatings*", in *Thermal Barrier Coating Workshop* (eds. Brindley, W. J.), 235-250, Cleveland, Ohio, March 27-29, 1995.

[10] Sidewell, C. V. and Cruse, T. A., "*Mechanical Testing Program for Thermal Barrier Coating Development*", Report 960801, 1996.

[11] Kokini, K., Takeuchi, Y. R. and Choules, B. D., "*Surface Thermal Cracking of Thermal Barrier Coatings owing to Stress Relaxation: Zirconia vs. Mullite*", Surface and Coating Technology, **82**, 77-82, 1996.

[12] Zhu, D. and Miller, R. A., "*Investigation on Thermal Fatigue Behavior of Thermal Barrier Coatings*", in *International Conference on Metallurgical Coatings and Thin Films, ICMCTF 97* San Diego, California, April 21-23, 1997.

[13] Luxon, J. T. and Parker, D. E., "*Industrial Lasers and Their Applications*", Prentice-Hall, Inc., Englewood Cliffs, New Jersey, 1985.

[14] Milonni, P. W. and Eberly, J. H., "*Lasers*", John Wiley & Sons, New York, 1988.

[15] Johnsen, B. P., Cruse, T. A., Miller, R. A. and Brindley, W. J., "*Compressive Fatigue of a Plasma Sprayed ZrO_2-8%Y_2O_3 and ZrO_2-10%NiCrAlY TTBC*", Journal of Engineering Materials and Technology, **117**, 305-310, 1995.

[16] Thurn, G., Schneider, G. A. and Aldinger, F., "*High-temperature Deformation of Plasma-sprayed ZrO2-Thermal Barrier Coatings*", Materials Science and Engineering, to be published, 1996.

[17] Liu, S.-Y. and Chen, I.-W., "*Fatigue of Yttria-Stablized Zirconia:II, Crack Propagation, Fatigue Striations, and Short-Crack Behavior*", Journal of the American Ceramic Society, **74**, 1206-1216, 1991.

[18] Dauskardt, R. H., James, M. R., Porter, J. R. and Ritchie, R. O., "*Cyclic Fatigue-crack Growth in a SiC-whisker-reinforced Alumina Ceramic Composite: Long- and Small-crack Behavior*", Journal of the American Ceramic Society, **75**, 759-771, 1992.

[19]   Dauskardt, R. H., Dalgleish, B. K., Yao, D., Ritchie, R. O. and Becher, P. T., *"Cyclic Fatigue-crack Propagation in a Silicon Carbide Whisker-reinforced Alumina Composite: Role of Load Ratio"*, Journal of Materials Science, **28**, 3258-3266, 1993.

[20]   Paris, P. C., Gomez, M. P. and Anderson, W. E., *"A Rational Analytic Theory of Fatigue"*, The Trend in Engineering, **13**, 9-14, 1961.

[21]   Murakami, Y., *"Stress Intensity Factors Handbook"*, 108, Pergamon Press, Oxford, 1987.

APPENDIX NOMENCLATURE

t_c, t_b and t_s — Ceramic coating, bond coat and substrate thicknesses, mm

α — Thermal expansion coefficient, m/m·°K

I_0 and I (r) — Laser irradiance or power density at the beam center and distance r from the center , MW/m²

P — Laser beam total power, W

k — Thermal conductivity, W/m·°K

ρ — Density, kg/m³

c — Heat capacity, J/kg·K

E — Young's Modulus, GPa

v — Poisson's ratio

σ^{th}, σ^{re} and σ^{total} — Thermal stresses, residual stresses and total stresses in coating systems, MPa

σ_{th} and σ_{th}^0 — Thermal stress and initial thermal stress in ceramic coating, MPa

T and ΔT — Temperature and temperature swing, °K

R — Gas constant, J/mol·°K

t and t_i — Time, sec.

A — Pre-exponential constant for ceramic coating creep

n — Stress exponent for ceramic coating creep

s — Time exponent for ceramic coating creep

Q — Activation energy for ceramic coating creep, J/mol

$\dot{\varepsilon}_p$ — Ceramic coating creep strain rate, 1/sec

ε_p — Ceramic coating creep strain

K_{max}, K_{min} and ΔK — Maximum and minimum stress intensity factors, and the stress intensity amplitude, of the crack, $MPa \cdot m^{1/2}$

ΔK_{1LCF} and ΔK_{1HCF} Mode I stress intensity factor amplitudes of the crack under low cycle and high cycle loads respectively, $MPa \cdot m^{1/2}$

C, C_1 and C_2 Constants

m, p and q Stress intensity exponents in fatigue, and $q = m + p$

N and N_{HCF}^* LCF cycle number and HCF characteristic cycle number

$a(i)$ Crack length at the ith cycle, mm

b_i Laser interaction depth, mm

P Concentrated load per unit thickness acting on the crack, N/m, $P = \sigma_{HCF} \cdot b_i$

Z and $f(i)$ Coefficients associated with the crack configuration

REPORT DOCUMENTATION PAGE

Public reporting burden for this collection of information is estimated to average 1 hour per response, including the time for reviewing instructions, searching existing data sources, gathering and maintaining the data needed, and completing and reviewing the collection of information. Send comments regarding this burden estimate or any other aspect of this collection of information, including suggestions for reducing this burden, to Washington Headquarters Services, Directorate for Information Operations and Reports, 1215 Jefferson Davis Highway, Suite 1204, Arlington, VA 22202-4302, and to the Office of Management and Budget, Paperwork Reduction Project (0704-0188), Washington, DC 20503.

1. AGENCY USE ONLY (Leave blank)	2. REPORT DATE May 1997	3. REPORT TYPE AND DATES COVERED Technical Paper

4. TITLE AND SUBTITLE

Influence of High Cycle Thermal Loads on Thermal Fatigue Behavior of Thick Thermal Barrier Coatings

6. AUTHOR(S)

Dongming Zhu and Robert A. Miller

5. FUNDING NUMBERS

WU–523–21–13
1L161102AH45

7. PERFORMING ORGANIZATION NAME(S) AND ADDRESS(ES)

NASA Lewis Research Center
Cleveland, Ohio 44135–3191
and
U.S. Army Research Laboratory
Cleveland, Ohio 44135–3191

8. PERFORMING ORGANIZATION REPORT NUMBER

E–10691

9. SPONSORING/MONITORING AGENCY NAME(S) AND ADDRESS(ES)

National Aeronautics and Space Administration
Washington, DC 20546–0001
and
U.S. Army Research Laboratory
Adelphi, Maryland 20783–1145

10. SPONSORING/MONITORING AGENCY REPORT NUMBER

NASA TP–3676
ARL–TR–1341

11. SUPPLEMENTARY NOTES

Responsible person, Dongming Zhu, organization code 5160, (216) 433–3161.

12a. DISTRIBUTION/AVAILABILITY STATEMENT

Unclassified - Unlimited
Subject Categories 23 and 24

This publication is available from the NASA Center for AeroSpace Information, (301) 621–0390.

12b. DISTRIBUTION CODE

13. ABSTRACT (Maximum 200 words)

Thick thermal barrier coating systems in a diesel engine experience severe thermal low cycle fatigue (LCF) and high cycle fatigue (HCF) during engine operation. In the present study, the mechanisms of fatigue crack initiation and propagation, as well as of coating failure, under thermal loads which simulate engine conditions, are investigated using a high power CO_2 laser. In general, surface vertical cracks initiate early and grow continuously under LCF and HCF cyclic stresses. It is found that in the absence of interfacial oxidation, the failure associated with LCF is closely related to coating sintering and creep at high temperatures, which induce tensile stresses in the coating after cooling. Experiments show that the HCF cycles are very damaging to the coating systems. The combined LCF and HCF tests produced more severe coating surface cracking, microspallation and accelerated crack growth, as compared to the pure LCF test. It is suggested that the HCF component cannot only accelerate the surface crack initiation, but also interact with the LCF by contributing to the crack growth at high temperatures. The increased LCF stress intensity at the crack tip due to the HCF component enhances the subsequent LCF crack growth. Conversely, since a faster HCF crack growth rate will be expected with lower effective compressive stresses in the coating, the LCF cycles also facilitate the HCF crack growth at high temperatures by stress relaxation process. A surface wedging model has been proposed to account for the HCF crack growth in the coating system. This mechanism predicts that HCF damage effect increases with increasing temperature swing, the thermal expansion coefficient and the elastic modulus of the ceramic coating, as well as the HCF interacting depth. A good agreement has been found between the analysis and experimental evidence.

14. SUBJECT TERMS

Thermal barrier coatings; Thermal high cycle and low cycle fatigue; Ceramic sintering and creep; Fatigue mechanisms

15. NUMBER OF PAGES
51

16. PRICE CODE
A04

17. SECURITY CLASSIFICATION OF REPORT Unclassified	18. SECURITY CLASSIFICATION OF THIS PAGE Unclassified	19. SECURITY CLASSIFICATION OF ABSTRACT Unclassified	20. LIMITATION OF ABSTRACT